Title
Neuromorphic Nanowire Networks as a Physical Substrate for In-Materio Reservoir Computing

Permalink
https://escholarship.org/uc/item/7m91m3q0

Author
Lilak, Samuel

Publication Date
2022

UNIVERSITY OF CALIFORNIA

Los Angeles

Neuromorphic Nanowire Networks as a Physical Substrate for In-Materio Reservoir Computing

A dissertation submitted in partial satisfaction of the requirements for the degree Doctor of Philosophy in Chemistry

by

Sam Lilak

2022

ABSTRACT OF THE DISSERATION

Neuromorphic Nanowire Networks as a Physical Substrate for In-Materio Reservoir Computing

by

Sam Lilak

Doctor of Philosophy in Chemistry

University of California, Los Angeles, 2022

Professor James K. Gimzewski, Chair

The past decade has seen a sharp rise in the development and manufacture of different hardware frameworks to meet the ever-rising computational demands of the machine learning software community. Conventional computing architectures require massive server farms and consume large quantities of energy to perform these tasks. Consequently, this necessitates that end users must connect wirelessly to powerful servers capable of performing complex machine learning tasks. The aforementioned shortcomings have sparked a pursuit for the development of energy efficient hardware capable of successfully performing complex computational tasks offline.

Self-organized nanowire arrays of memristive materials, known as atomic switch networks, are the collection of billions of individual memristive elements randomly intertwined as an interconnected network of electrically active junctions. The resulting morphology of the network has a number of attractive neuromorphic properties and emergent phenomena which yield an intrinsic capacity to perform complex computational tasks on a physical substrate. Under an external stimulus these networks exhibit a dynamic, non-equilibrium modulation of conductance across the entire network. The resultant non-linear dynamics are capable of being utilized as both logic and memory components operating in parallel through a technique called in-materio computing. This form of computing enables a physical substrate to be utilized as a dynamic reservoir capable of transforming a simple external stimulus into higher dimensional non-linear outputs. The output layer is then mapped onto a desired computational task through a technique called reservoir computing (RC). Silver selenide (Ag_2Se) and silver iodide-based (AgI) nanowire networks were characterized and implicated as efficient memristive materials for RC applications. Both materials were successfully employed within an RC framework for waveform regression, spoken digit recognition and handwritten digit classification tasks.

Conventional techniques for nanoscale manufacturing have also begun to hit their limit of resolution, garnering interest in developing new techniques capable of manufacturing materials with molecular and/or atomic precision. Atomically precise manufacturing (APM) aims to implement scanning probe microscopy techniques in conjunction with tailor made molecular tools as a powerful system capable of realizing atomic scale 3D printing. The preliminary state of APM is explored using molecular tools for the abstraction/donation of individual atoms.

The dissertation of Sam Lilak is approved.

Subramanian S. Iyer

Richard Kaner

Yves Rubin

James K. Gimzewski, Committee Chair

University of California, Los Angeles

2022

Sometimes I think it is a great mistake to have matter that can think and feel. It complains so. By the same token, though, I suppose that boulders and mountains and moons could be accused of being a little too phlegmatic. – Kurt Vonnegut

Table of Contents

List of Figures

Figure 14. Reservoir's spoken digit accuracy of 95% across all possible voltage ranges of the DAC. (Right) Regression of the input layer shows overfitting with increasing points for regression while the reservoirs accuracy improves.

Figure 15. Raw audio data of speaker Jackson saying the digit zero.

Figure 16. (Top) The MFCC converted signal of the raw audio data as voltage time-series to be fed into the network. (Bottom) Readout layer response of all 14 electrodes in response to the stimulus shows unique dynamic transformations of the parent signal.

Figure 17. The Ag_2Se network's accuracy was 85% across all ten digits from a single speaker with equal accuracy in recalling information of previous inputs. The F1 score represents the mean harmonics between recall and precision. (Right) Accuracies of 82% were achieved in classifying a single spoken digit across six speakers with comparable recall and precision.

Figure 18. (Left) Accuracy of MNIST classification as a function of number of digits used for training and readout layers used demonstrates 92% accuracy after 2000 digits. (Right) Maximum accuracy of MNIST as a function of readout layers used shows a saturation of accuracy with 7 electrodes.

Figure 19. (Left) MI between all electrodes showing heat map regions of higher mean mutual information. A linear increase in accuracy as a function of MI can be observed from individual readout electrodes suggesting more dynamic channels have better accuracies. (Right) The Lissajous plots exhibiting non-linear dynamics from Figure X. appear to directly map onto regions of higher MI.

List of Tables

List of Symbols and Acronyms

ADC	Analog to Digital Converter
AgI	Silver Iodide
Ag_2S	Silver Sulfide
Ag_2Se	Silver Selenide
ANN	Artificial Neural Networks
APM	Atomically Precise Manufacturing
ASN	Atomic Switch Network
BATT	1-Bromo-3,5,7-tris(mercaptomethyl)adamantane
CNN	Convolution Neural Network
DAC	Digital to Analog Converter
DAQ	Data Acquisition
e-Beam	Electron Beam
EDS	Energy-Dispersive X-Ray Spectroscopy
FSDD	Free Spoken Digit Database
GPU	Graphics Processing Unit
MEA	Multielectrode array
MFCC	Mel-Frequency Cepstrum Coefficient
MI	Mutual Information

NI	National Instruments
NMP	N-methyl-2-pyrrolidone
PXI	PCI eXtensions for Instrumentation
PXIe	PCI eXtensions for Instrumentation Express
RC	Reservoir Computing
SEM	Scanning Electron Microscopy
SMU	Source Measurement Unit
STM	Scanning Tunneling Microscopy
TEM	Transmission Electron Microscopy
UV-Vis	Ultraviolet-Visible Spectroscopy
XRD	X-Ray Diffraction
XPS	X-Ray Photoelectron Spectroscopy

Acknowledgements

I am eternally grateful for the doors of knowledge that I've had the privilege to open during my tenure as a graduate student.

Jim you have been the most fascinating mentor and your patience and dedication to working with me has been nothing short of an incredible journey into pushing the limits of the sciences. I cannot thank you enough for the time you have spent guiding me throughout my graduate career and preparing me for entering the professional work force. Jim, you are truly one of a kind, unlike anyone I've ever met before and I feel privileged to have had the opportunity to work alongside you.

Adam Stieg, your wisdom and guidance has been instrumental in aiding my development of the various skill sets I've picked up along the way. Words cannot express the gratitude I have for all the time, patience and knowledge you've endowed unto me.

To those of my cohort with whom we've shared many pleasant social distractions from our studies, I thank you for all the great times and wish you all the best in your future endeavors.

I would like to thank all of the past and present members of the Gimzewski lab. The foundation you've contributed to is truly nothing short of a testament to the beauty of the sciences as a consequence of rigorous collaboration.

Lastly, I would like to thank my family. Your boundless depths of love and support have kept me afloat through thick and thin and I love you all.

Vita

2013-2015	Research Assistant Department of Chemistry University of North Dakota, Grand Forks, ND
2015	B.S. in Chemistry University of North Dakota Grand Forks, ND
2015-2019	Teaching Assistant Department of Chemistry and Biochemistry University of California, Los Angeles, CA
2016-2021	Art|Sci Center Instructor California NanoSystems Institute University of California, Los Angeles, CA

Publications

1. Kotooka, T., Lilak, S., Stieg, A., Gimzewski, J., Sugiyama, N., Tanaka, Y., Tamukoh, H., Usami, Y., & Tanaka, H. *Ag2Se Nanowire Network as an Effective In-Materio Reservoir Computing Device*. (pre-print)

2. Dunham, C. S., Lilak, S., Hochstetter, J., Loeffler, A., Zhu, R., Chase, C., Stieg, A. Z., Kuncic, Z., & Gimzewski, J. K. Nanoscale neuromorphic networks and criticality: a perspective. *Journal of Physics: Complexity*, *2*(4), 042001. (2021)

3. Lilak, S., Woods, W., Scharnhorst, K., Dunham, C., Teuscher, C., Stieg, A. Z., & Gimzewski, J. K. Spoken Digit Classification by In-Materio Reservoir Computing With Neuromorphic Atomic Switch Networks. *Frontiers in Nanotechnology*, *3*, 38. (2021)

4. Shokeen, B., Zamani, L., Zadmehr, S., Pouraghaie, S., Ozawa, R., Yilmaz, B., Lilak, S., Sharma, S., Ogawa, T., Moshaverinia, A., & Lux, R. Surface Characterization and Assessment of Biofilm Formation on Two Titanium-Based Implant Coating Materials. *Frontiers in Dental Medicine*, *2*. (2021)

5. Aguilera, R.; Scharnhorst, K.; Lilak, S.L.; Dunham, C.S.; Aono, M.; Stieg, A.Z.; Gimzewski, J.K. Atomic Switch Networks for Neuroarchitectonics: Past, Present, Future. *Advances in Atom and Single Molecule Machines*; Springer Nature (2020).

6. Tan, S., Wu, X., Xing, Y., Lilak, S., Wu, M., & Zhao, J. X. Enhanced synergetic antibacterial activity by a reduced graphene oxide/Ag nanocomposite through the photothermal effect. Colloids and Surfaces B: Biointerfaces, 185, 110616 (2019).

7. Andrianova, A. A., Yeudakimenka, N. A., Lilak, S. L., Kozliak, E. I., Ugrinov, A., Sibi, M. P., & Kubátová, A. Size exclusion chromatography of lignin: The mechanistic aspects and elimination of undesired secondary interactions. Journal of Chromatography A, 1534, 101–110 (2018)

Chapter 1:

Introduction

Machine learning applications have become ubiquitous in everyday life and are readily accessible to your average individual[1,2]. There is currently a large demand for increasing the efficiency of these machine learning algorithms coupled with the desire for them to process ever increasing sizes of datasets[3]. Consequently, this has imposed a massive computational burden on the training costs and modern compute architectures have not been able to keep pace with the steep rise in demand[3]. Current computing architectures which are employed for machine learning tasks require access to prohibitively expensive large arrays of supercomputers which consume massive amounts of energy to achieve higher accuracies. Because end users don't have access to such hardware, this necessitates that they have access to a wireless connection in order to carry out their desired machine learning tasks which consequently cannot be utilized in remote environments. Of even more concern is the sharp rise in computing power demands which have skyrocketed within the last decade[3]. These demands have sparked environmental concerns and recently debates on policy considerations that should be accounted for in curbing machine learning's carbon footprint[4,5]. It has been postulated that at the current rate of machine learning trends that the ImageNet dataset could be classified with an error rate of just 5%. While this sounds impressive it would come at the cost of requiring 10^{18} billion floating-point operations which would generate an estimated 10 billion pounds of CO_2, roughly the same amount generated by the entirety of New York City in one month without green energy sources[6].

To fully understand the current limitations of machine learning algorithms we need to consider the hardware employed to carry out these operations. Prior to 2012, most machine learning tasks employed the central processing unit of computers to drive the algorithms[3]. Graphics processing units (GPU) emerged as an efficient alternative due to its parallel processing capabilities at the cost of higher energy consumption[7]. Since the advent of GPU driven algorithms in 2012, the computing power demands have doubled every 3.4 months. That rate has further risen since 2016 to doubling every 2 months[3,8]. This is a stark contrast to the pre-2012 era of Moore's Law in which computing power demands had doubled every 2 years since 1985 and it's likely that these power demands will continue to increase at an accelerated rate if new hardware frameworks aren't developed. Current computing architectures are based on a Von Neumann design which is comprised of separate processing and memory elements. The separation of hardware elements requires hardware for bussing information between the two. Consequently, even the most efficiently optimized processing units are going to be limited by the rate at which information can be bused between it and the memory component. This fault in modern architectures is called the Von Neumann bottleneck and it has sparked the search for a new hardware element capable of performing both memory and logic operations in parallel[9–11].

Memristive frameworks are one such promising candidate to achieve parallel computing. A memristive material exhibits a dynamic, non-linear response to an input stimulus as shown in Figure 1[12,13]. This unique, dynamic response has the intrinsic capacity to be harnessed as both logic and memory elements. Logic elements are typically represented as a binary 0 or 1 which could correspond to the low (OFF) and high (ON) conductance states respectively. However, memristive materials exhibit quantized conductance states and the most advanced realization of a multibit memristive material has exhibited 92 stable bits[14]. This is similar to the interest in using qbits in quantum computing to represent non-binary bits and is a highly desired property for different algorithmic approaches[15]. Likewise, the ON state usually has a specific lifetime or memory component to it. This fading memory can exist as both volatile and non-volatile states dependent on the input stimulus as an analogy to short- and long-term memory respectively[16,17].

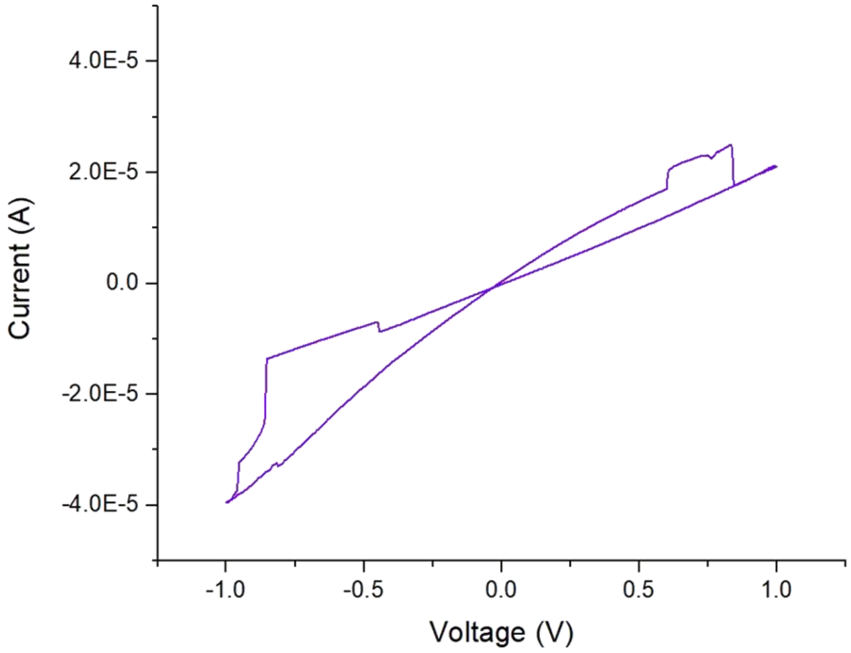

Figure 1. The non-linear current-voltage response of a silver selenide nanowire network biased by a 1 V, 1 Hz triangle wave.

The first physical realization of a memristive material was achieved in 2008 at Hewlett-Packard by Stanley Williams[13,18]. Since that time there has been an explosion in interest in developing new memristive materials and hardware frameworks for them to be implemented in[19]. The two common architectures explored to date are crossbar arrays and atomic switch networks[20–22]. Crossbar arrays aim to leverage individual memristive elements with absolute control over every single element in the array which is analogous to tuning the individual synaptic weights in modern artificial neural network (ANN) algorithms implemented in software[23,24]. Atomic switch networks (ASN) on the other hand aim to leverage the self-organization of randomly intertwined memristive elements and the behavior that emerges as a consequence[25,26]. While there is merit to the utilization of both architectures, this work focuses on the ASN framework as a suitable substrate for parallel computing.

Modern ANNs typically require the weighting of every synaptic connection within the algorithm (or crossbar) with each weight adding to the computational burden on the system[27]. A modified ANN approach called reservoir computing employs a dynamic reservoir algorithmically which transforms simple input signals into a higher dimensional phase space[28]. This dynamic transformation generates a complex output layer which is the only layer used for weighting in RC, greatly reducing the computational training costs[29].

Historically the reservoirs for RC applications were all created algorithmically in software (Figure 2.), however recent advances began employing physical reservoirs such as liquids and memristive materials[29,30]. Given the memristive properties of materials within an ASN framework, the ASN is implicated as a suitable physical substrate with the intrinsic capacity to perform computational tasks[31–33]. Leveraging the innate ability for the ASN to perform computations physically, or in-materio, further reduces the training costs of modern software-based RC frameworks. The effectiveness of the ASN as an in-materio RC substrate has been demonstrated through the successful classification of spoken and handwritten digit tasks[31].

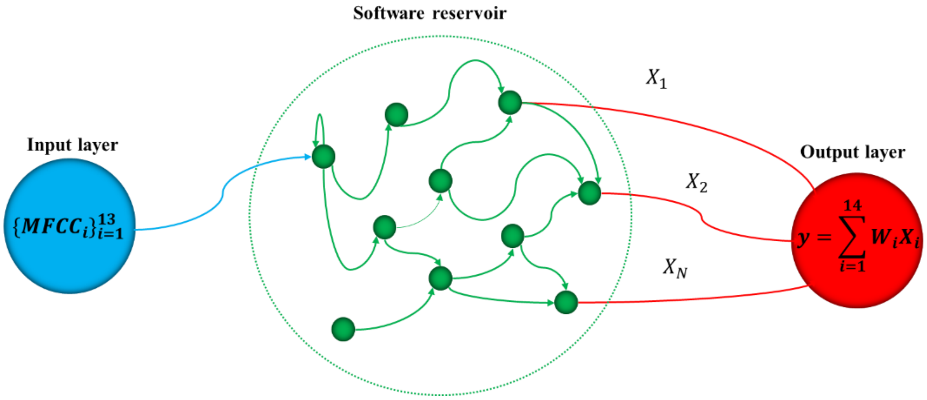

Figure 2. Schematic representation of software-based RC. A simple input layer (blue) is fed into a dynamic reservoir (green) which transforms the input into a higher dimensional space. Connections between green nodes would normally be weighted in a traditional ANN. Through RC, only the output layer (red) is weighted and used for linear regression-based training.

In addition to the desire for new compute frameworks to address the aforementioned limitations of modern computing architectures, there is a great demand to improve the limits of resolution when manufacturing these materials. Conventional techniques for manufacturing nanoscale materials like extreme ultraviolet lithography have begun to reach their fundamental limits, though research in the field to surpass these limits is still ongoing[34,35]. Scanning probe microscopes are a promising form of instrumentation for additive manufacturing techniques capable of achieving atomic scale resolution. Through a technique known as atomically precise manufacturing this work explores the proof of concept process of using tailor made molecular tools in conjunction with a scanning tunneling microscope (STM) to fabricate atomically resolved 3D structures.

Chapter 2:

Neuromorphic Atomic Switch Networks

2.1 Material Development and History

Interest in atomic switch networks originated from Masa Aono's seminal paper on the quantized conductance observed in an isolated silver sulfide (Ag_2S) nanowire in 2005[36]. This work ultimately led to a collaboration with James K. Gimzewski and together they fabricated the first brain inspired, neuromorphic silver sulfide atomic switch networks in 2012[20]. These networks consequently demonstrated an array of fascinating dynamic electrical properties which were further explored. These networks exhibited short- and long-term memory properties in addition to higher harmonic generation from the non-linear transformations of simple input signals[20,37]. The ASN was first implicated as a suitable substrate for RC a year later via simulations[38]. In 2016 a physical network successfully realized waveform generation from a simple sinusoidal input signal in an RC framework[33]. It has since been implicated as a suitable substrate for additional RC applications including temporal logic operations, spoken digit classification and handwritten digit classification techniques[31,32].

Exploration of new classes of materials in addition to Ag_2S began in 2018 as a proof of concept that this framework could be expanded upon (Figure 3.). Silver iodide nanowires emerged as a promising candidate which could easily be implemented into the existing underlying architecture with minimal modifications. In the 2021 they were successfully utilized in an RC framework for spoken digit recognition tasks using publicly available audio data[31]. Recent works have explored silver selenide as a robust, stable switching material inspired by commercially available single element memristors. Like its predecessors, Ag_2Se networks have been implemented as a suitable RC framework for spoken digit and handwritten digit classification tasks[39].

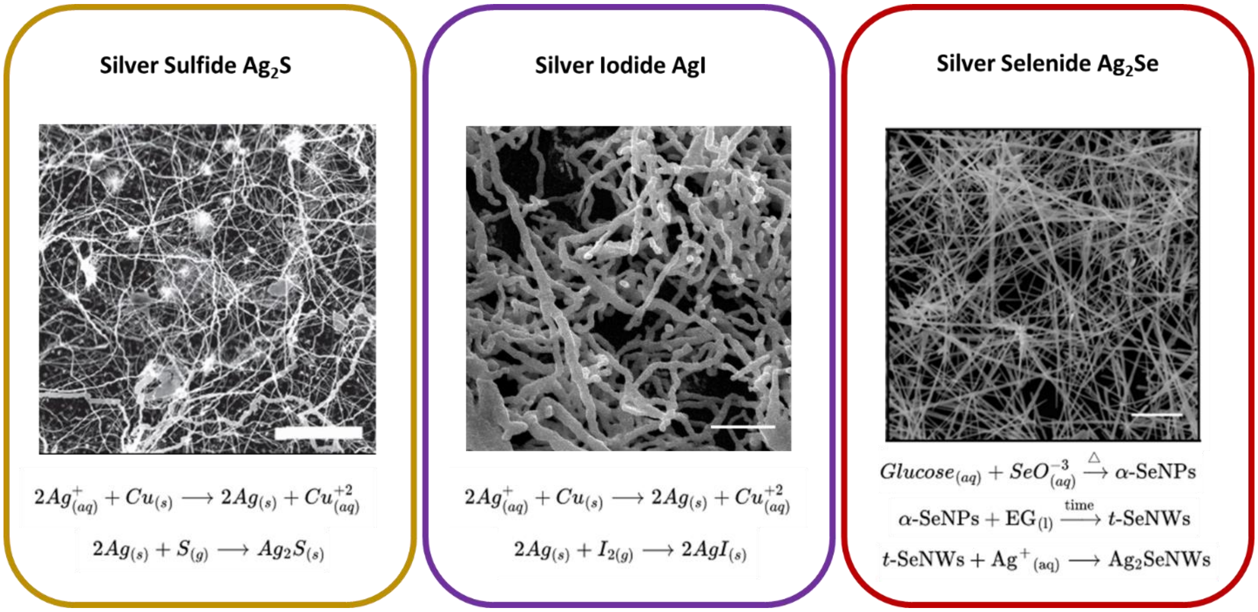

Figure 3. Schematic overview of the history of ASN material development overtime (scale bars of 50 µm, 20 µm and 5 µm from left to right).

2.2 Device Fabrication

Custom 16 electrode multielectrode arrays (MEA) were fabricated in a clean room environment on 4” silicon wafers. The wafers were first thermally passivated with a 500 nm oxide layer. The 4x4 grid of electrodes was patterned using optical lithography in conjunction with an nLOF-2020 photoresist. Platinum electrodes were then deposited using electron beam (e-beam) evaporation of Cr(5nm)/Pt(150nm) with chromium acting as a wetting layer to facilitate better adhesion to the wafer. Chemical liftoff was carried out overnight using n-methyl-2-pyrrolidone (NMP) as a solvent. The inner electrodes were spaced 200 µm apart with diameters of 30 or 50 µm. A 400 nm layer of SU-8 was then spin coated onto the wafer and lithographically patterned to make point contacts on the inner electrodes. The SU-8 was hard baked to create a permanent, insoluble layer. Finally, 5 µm diameter grids spaced 5 µm apart were then lithographically patterned over the inner electrodes using optical lithography and an nLOF-2020 photoresist. These grids were used to deposit 300 nm of copper via e-beam lithography to serve as seed sites for the electroless growth of silver nanowires. Chemical liftoff of copper was also carried out overnight with NMP as a solvent. Each 4” wafer yielded 16 suitable MEAs for the growth or drop casting of nanowires.

2.3 Silver Iodide Synthesis

Silver nanowires were synthesized through an electroless deposition technique[40]. The 16 electrode MEA was immersed in a 20 mL 50 mM $AgNO_3$ solution for 30 minutes in which the copper grid was optically converted to a lustrous silver as shown in equation 1.

$$Cu_{(s)} + 2Ag^{+}_{(aq)} \rightarrow Cu^{+2}_{(aq)} + 2Ag\,NWs \qquad (1)$$

Resistance measurements were then carried out to ensure sufficient conductivity (connectivity) between all possible electrode permutations. Silver iodide nanowires were then synthesized by suspending the silver nanowire chip over an iodine pellet in an ultrahigh purity nitrogen atmosphere. The iodine pellet was heated to 30^{o} C for 2 minutes and the exposure to the iodine gas immediately resulted in a visually apparent tarnishing of the silver nanowires as shown in equation 2.

$$2Ag\,NWs + I_{2(g)} \longrightarrow 2AgI\,NWs \qquad (2)$$

The formation of silver iodide was confirmed by using transparent thin films of silver sputter coated onto a glass microscope slide for ultraviolet-visible (UV-Vis) spectroscopy and X-ray photoelectron spectroscopy (XPS) experiments as shown in Figure 4. The absorbance maximum at 424 nm is in good agreement with previously reported AgI spectra[41,42]. XPS revealed the presence of iodine $3d_{5/2}$ and $3d_{3/2}$ at 620 eV and 631 eV respectively which is consistent with the presence of I^- in AgI materials[43].

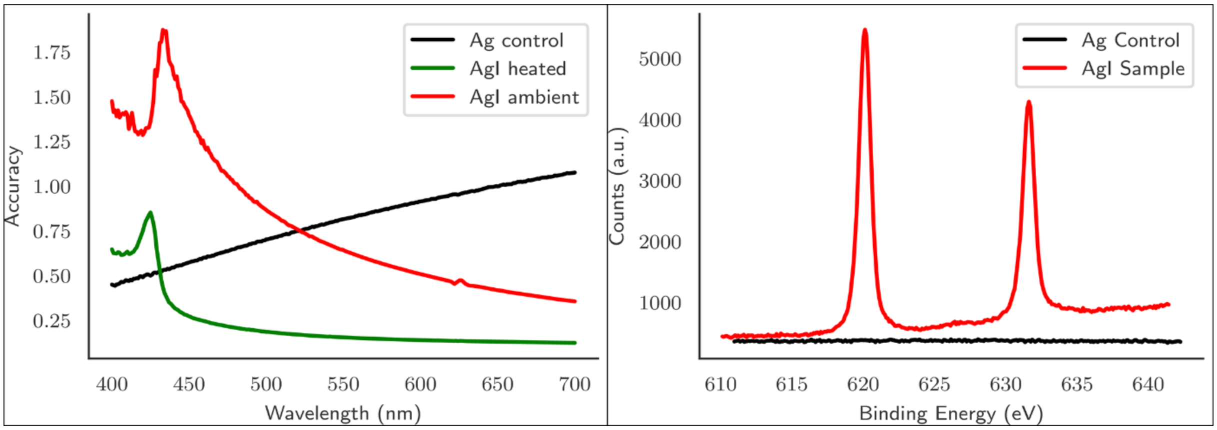

Figure 4. UV-Vis spectra (left) show a maximum at 424 nm confirming the presence of AgI formation from Ag thin films. The broad peak of the Ag control is a surface Plasmon from small Ag island in the thin film. XPS spectra of iodine's core levels $3d_{5/2}$ (620 ev) and $3d_{3/2}$ (631 eV) post-iodization are shown and indicative of I^- in AgI crystals.

2.4 Silver Selenide Synthesis

The preparation of silver selenide nanowires was performed through the synthesis of selenium nanowires which were drop cast onto an MEA without SU-8 derived point contacts to serve as a template for silver selenide. Selenium nanoparticles were first prepared in a hydrothermal reaction in which a 5.96 mM Na_2SeO_3 and $1.67 * 10^{-1}$ M glucose solution was prepared in 20 mL fresh DI water[44]. The solution was then heated to 180^o C for 30 minutes. During the nanoparticle formation process the clear solution turned to a turbid brick red color indicating the reduction of the selenite ion into α-Se nanoparticles as shown in equation 3.

$$Glucose_{(aq)} + SeO^{-3}_{(aq)} \xrightarrow{\triangle} \alpha\text{-Se NPs} \qquad (3)$$

The α-Se nanoparticles were then purified by centrifuging 1.5 mL aliquots at 13.4 kRPM for 10 minutes with fresh DI water and subsequent removal of the supernatant in triplicate. The purified red pellet was then suspended in 1.5 mL of ethylene glycol and sonicated for 45 seconds to agitate the solution and initiate the nanowire growth process. The ethylene glycol solution is then stored in the dark for a minimum of 3 days during which time a solid-solution-solid precipitation reaction begins to occur. The α-Se is partially soluble in ethylene glycol solutions and upon saturation begins to precipitate onto the colloidal nanoparticles acting as seed sites which yields trigonal nanowires[45] as shown in equation 4 and the scanning electron microscope (SEM) images in Figure 5.

$$\alpha\text{-Se NPs} + \text{Ethylene Glycol}_{(l)} \xrightarrow{\text{time}} t\text{-Se NWs} \qquad (4)$$

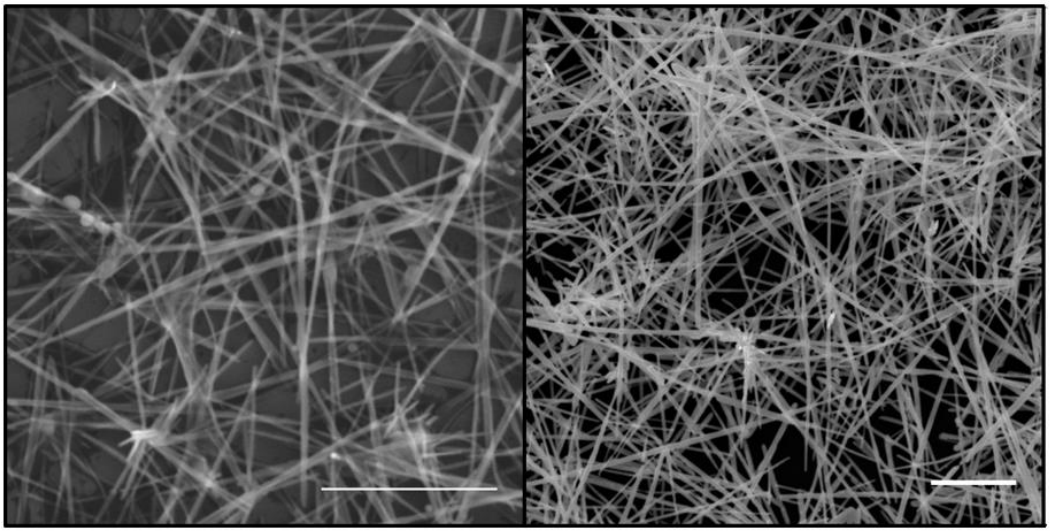

Figure 5. SEM images confirming the morphology of ethylene glycol synthesized nanowires (both scale bars are 5 µm).

Ag_2Se nanowires were also prepared using isopropanol and their morphology is shown both in SEM and transmission electron microscope (TEM) images in Figure 6. These nanowires are then drop cast onto the inner electrodes of an MEA and the formation of silver selenide was carried out by immersing the MEA into a 30 mL 50 mM $AgNO_3$ solution for 3 hours (equation 5).

$$t\text{-Se NWs} + 2\,\text{Ag}^{+}{}_{(\text{aq})} \longrightarrow \beta\text{--Ag}_2\text{Se NWs} \qquad (5)$$

The formation of ß-silver selenide was confirmed by X-ray diffraction (XRD) and energy-dispersive X-ray spectroscopy (EDS) techniques also shown in Figure 6.

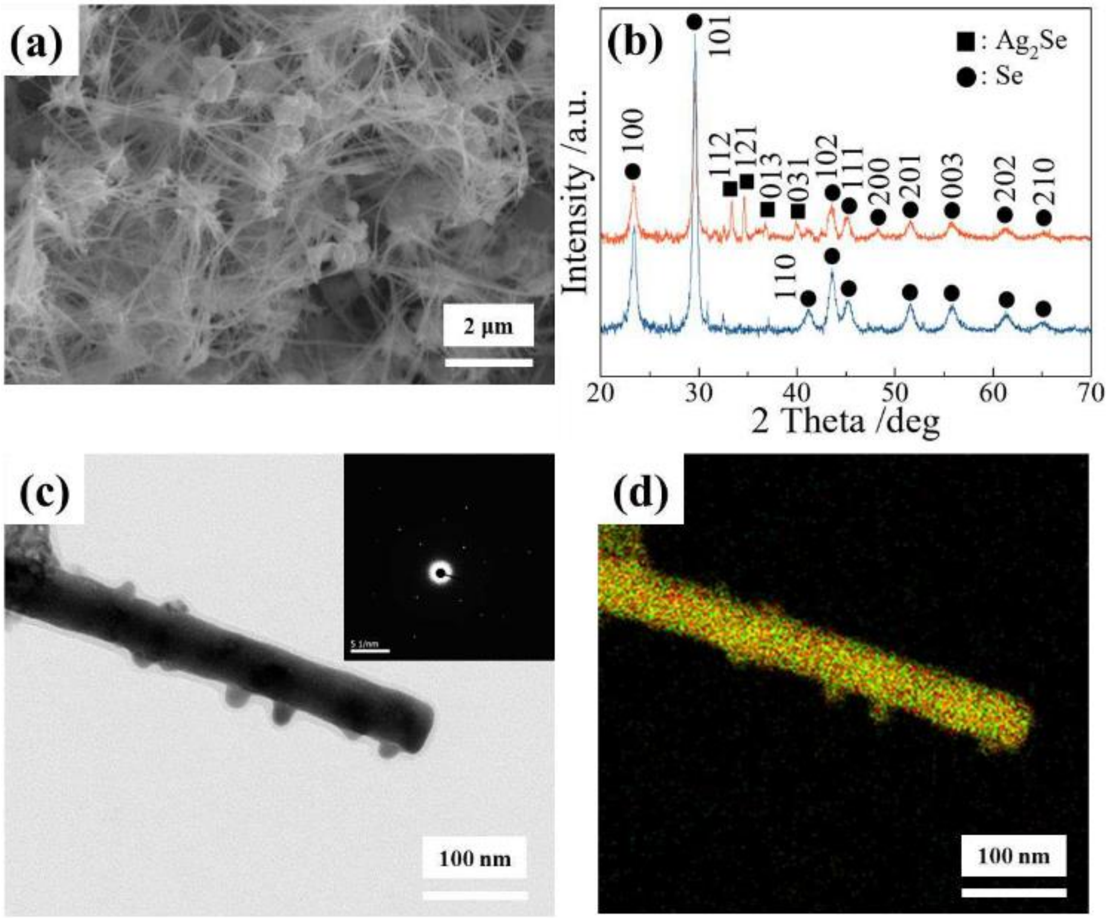

Figure 6. (a) SEM image showing morphology of the isopropanol nanowires (b) XRD confirms the initial presence of Se (blue line) and the conversion to Ag_2Se (orange line) through a templated reaction (c) TEM image of a single nanowire and its corresponding diffraction pattern (d) EDS analysis confirms a 2:1 Ag to Se stoichiometric ratio in the Ag_2Se nanowires.

2.5 In-Materio Reservoir Computing

There are four criteria that a physical reservoir must meet to be suitable for RC applications[29]: high dimensionality, non-linearity, fading memory and a separation property. High dimensionality is essential for its capability to map a simple input into a higher dimensional space which enables the readout of spatiotemporal dependencies from the parent signal when employing prediction tasks. Non-linearity is essential for the classification of systems that are conventionally only linearly separable[46]. The non-linear transformations of input signals enable those complex systems to become linearly separable with the XOR task as prime example[32,47]. The network must also exhibit a fading memory of previous inputs. Fading memory enables temporal correlations of recently input data without the system retaining memory of all past inputs. This is essential when analyzing time-series data with short-term dependencies. Finally, the network must have a separation property such that different reservoir signals can be separated into different classes. A modified schematic detailing in-materio RC in contrast to software based RC is shown in figure 7.

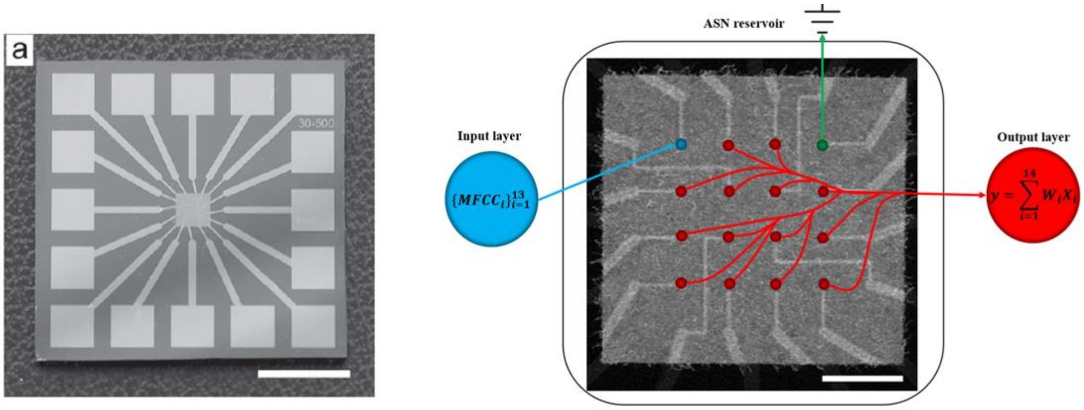

Figure 7. (Left) Optical image of the 16 electrode MEA with an electrolessly grown silver nanowire network (scale bar = 4 mm). (Right) Schematic of in-materio RC in which a simple input signal (blue) is non-linearly transformed throughout a dynamic network and weighting is only performed at the readout layer (red, scale bar = 600 µm).

Previous Ag_2S based ASNs have successfully exhibited the necessary criteria for RC and have been implemented into RC frameworks for both temporal logic operations and waveform regression[31–33]. Logic operations and waveform regression tasks were used as benchmarks to assess the suitability AgI and Ag_2Se based networks as substrates for in-materio RC tasks.

For logic operations, the XOR task was chosen due to the fact that its outputs are not linearly separable. This is of interest because many machine learning classifiers rely on the linear separation of different features to be isolated and classified. Successfully implementing the XOR task would implicate the networks as being capable of a higher order degree of separation. To perform the XOR task, two unipolar, arbitrary square wave pulses were fed into the network. The voltage pulse corresponds to a bit value of 1 and the 0 V regions correspond to a bit value of 0. Different voltages and frequencies were explored to discern the optimal conditions for RC. Linear regression was performed on the input layer (I), the output layer (N) and both layers combined (full reservoir R) to discern the accuracy of the XOR task. The non-temporal XOR task was able to achieve 100% accuracy with high fidelity at lower frequencies as shown in Table 1.

Table 1. Non-temporal accuracy of the XOR task in an AgI network with voltage pulses of 0.3 V and 3 V at input frequencies of 10 Hz and 5 kHz. Both the output layer (N) and full reservoir (R) show a significant improvement in accuracy over regressing the input layer (I) alone.

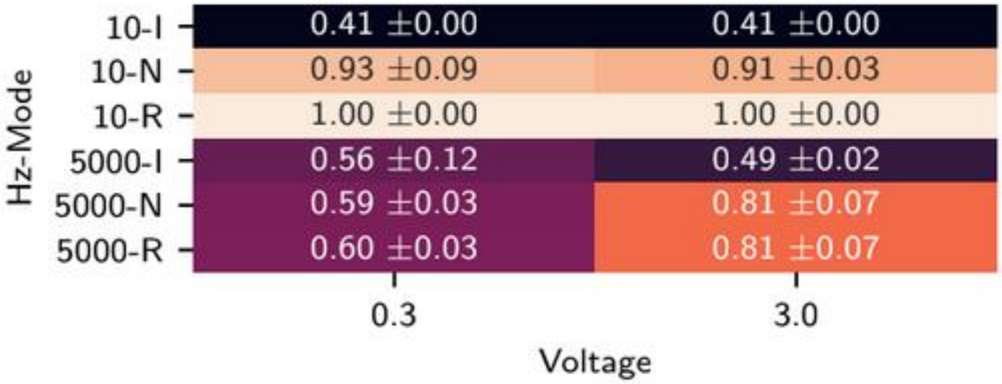

Hz-Mode	0.3	3.0
10-I	0.41 ±0.00	0.41 ±0.00
10-N	0.93 ±0.09	0.91 ±0.03
10-R	1.00 ±0.00	1.00 ±0.00
5000-I	0.56 ±0.12	0.49 ±0.02
5000-N	0.59 ±0.03	0.81 ±0.07
5000-R	0.60 ±0.03	0.81 ±0.07

Because RC relies on the manipulation of time-series data, it is paramount for the network to exhibit memory properties in addition to the non-linear dynamics. To assess the network's memory capabilities, recall of previous inputs was explored as shown in Figure 8. The lower frequency 10 Hz series of experiments only had a pattern length of 5, meaning only 4 possible bits of memory could be recalled. Despite this, the network demonstrated 100% accurate recall of previous XOR inputs in that limited dataset. The 5 kHz signal performed demonstrably worse, likely due to capacitive effects present in the AgI networks. At higher frequencies the non-linear behavior of the system becomes dominated by capacitance and is no longer effective as a dynamic reservoir. These results implicate the AgI networks as a suitable substrate for in-materio RC based applications.

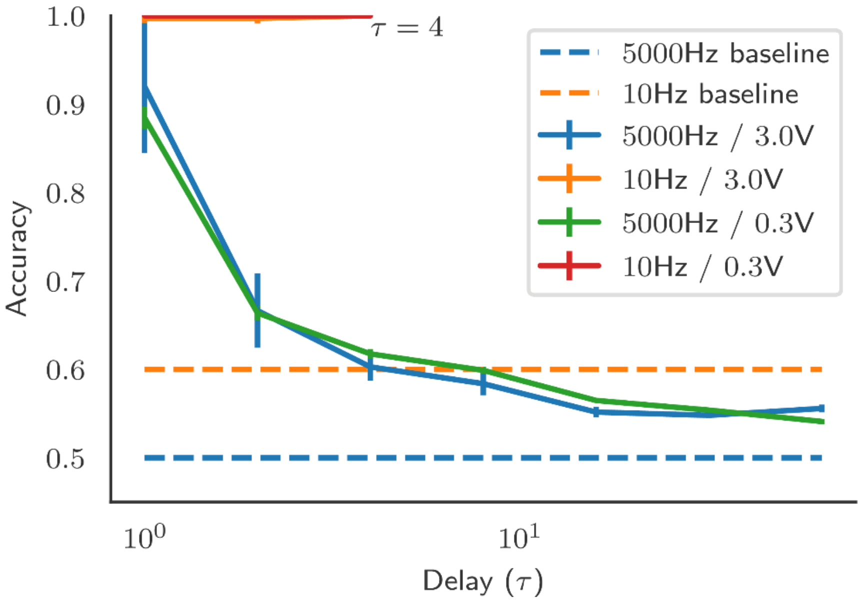

Figure 8. Recall of the XOR input signal τ bits in the past demonstrates 100% accuracy at lower 10 Hz frequencies, though accuracy quickly degrades at higher frequencies due to being dominated by capacitive effects.

Waveform regression tasks were carried out on the Ag_2Se networks to assess their suitability for RC applications. To do so, a simple 1 V, 11 Hz sinusoidal wave was fed into the network with two readout electrodes. Several different waveforms were learned through ridge regression as shown in Figure 9. The high accuracy of cosine and triangle waves is attributed to their similarities to the parent signal and are considered easier tasks. The lower performance of the sawtooth and square waves is a consequence of their relative complexity and higher frequency components innate to those signals. Nonetheless the incredibly high accuracy of the cosine and triangle waves exceeds the literature values previously reported in the Ag_2S networks and further implicated Ag_2Se as yet another suitable material for in-materio RC.

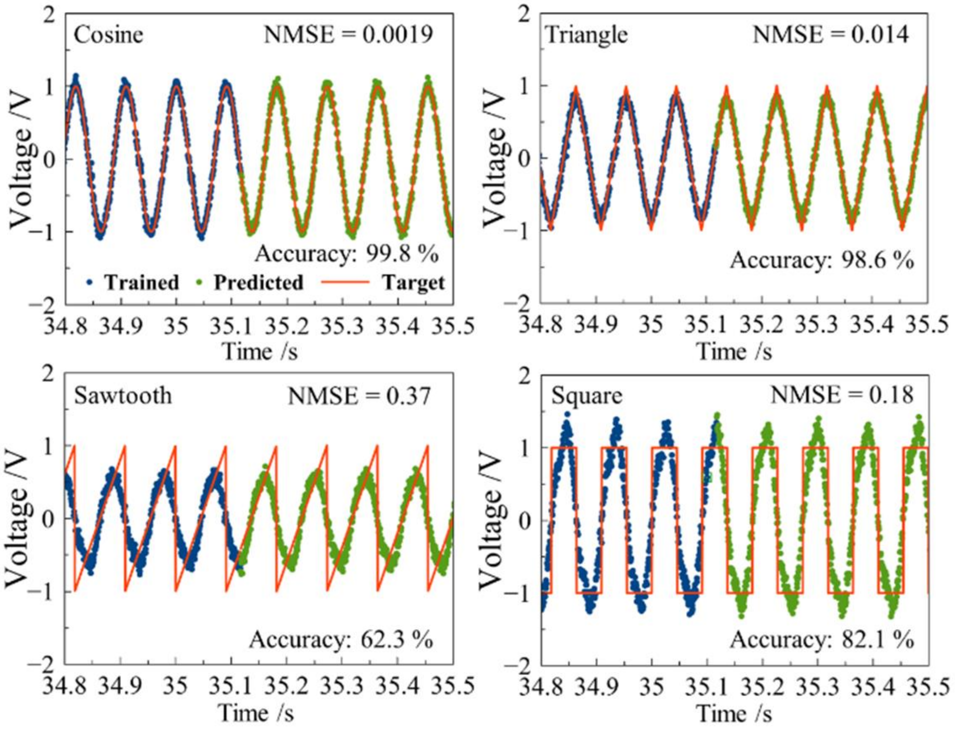

Figure 9. Waveform regression accuracies of the Ag_2Se networks demonstrates over 98.6% accuracy in the relatively easier cosine and triangle wave tasks while still offering some notable degree of accuracy in the significantly more difficult sawtooth and square wave tasks.

Chapter 3:

Electrical Characterization Methods

3.1 Hardware Overview

Electrical measurements were performed with National Instruments (NI) hardware using a NI-6368 direct acquisition (DAQ) in conjunction with a NI-4141 source measurement unit (SMU) and a PXI-2523 16x32 switch matrix. The DAQ is a 16-bit analog to digital converter (ADC) that also acts as 16-bit digital to analog converter (DAC) capable of both measuring and driving voltage signals simultaneously. The ADC was used to measure voltage traces at all 16 electrodes in addition to the DAC sourcing voltage signals as desired. Wiring from the DAQ to the device was routed through shielded connector boxes (SCB-64) to reduce electrical noise in the system. The SMU was employed as a sink used to measure current at the desired electrode. Signals could be routed as desired through any possible electrode permutation through the switch matrix. Wires are delivered from the switch matrix into a custom 3D printed sample holder capable of interfacing with our MEAs as shown in Figure 10. All of the PXI(e) cards are connected to a PXIe-1078 chassis. The PXIe chassis is highly modular in nature and can accommodate numerous additional forms of hardware as needed.

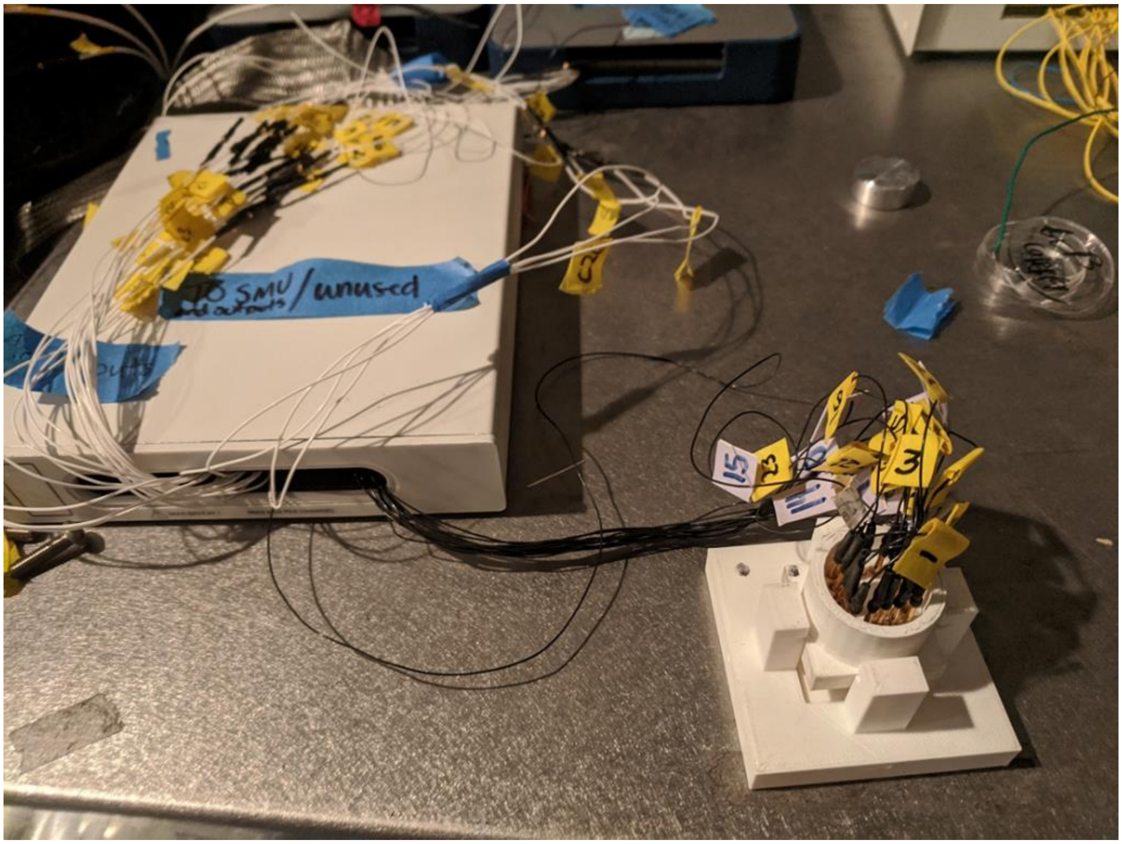

Figure 10. Visualization of wiring from SMUs and DAQs routed into the switch matrix (white wires, left) and wires then routed into the custom sample holder (black wires, right) which uses gold push pin electrodes to lock the holder firmly against the MEA's electrodes.

3.2 LabVIEW Software Suite Overview

A custom made LabVIEW software suite was programmed to interface with the NI hardware. This program enables users to work with a graphical user interface with which they can programmatically design experiments to suit their custom needs. The system is capable of outputting standard AC and DC waveforms in addition to spike pulses and variable noise based signals. Additionally, users can create arbitrary waveforms from external worksheets. This technique will be essential for the pre-processing of classification data to be fed into the network in the preceding chapters. The software also displays current, voltage and current-voltage traces to give the user a real-time visualization of the dynamics at play within the network. The 16x32 switch matrix enables users to route a signals through any possible electrode permutation as desired. Users are also able to save large switch matrix layouts for performing long-term experiments over days or even weeks. The system is fully automated and once all parameters have been tuned to the users liking they can set it and forget until the software terminates the experiment. A representative graphical interface of a sinusoidal wave being driven through the network is shown in Figure 11.

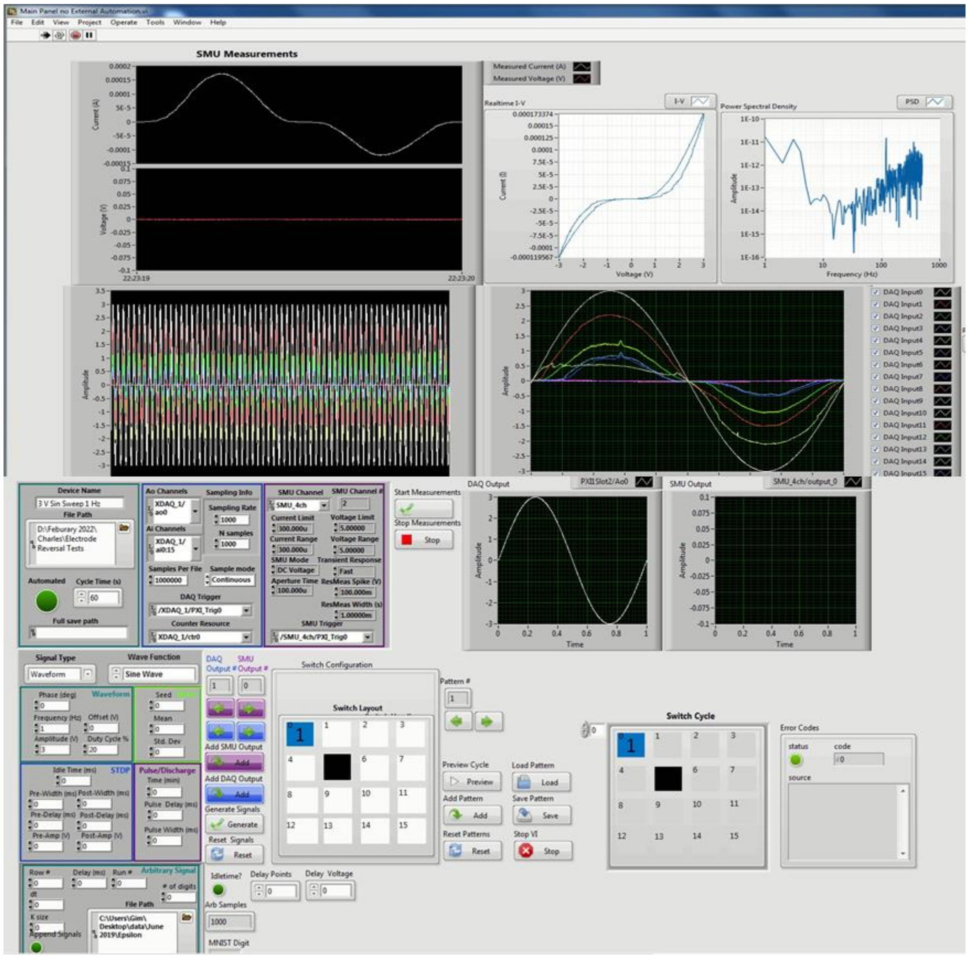

Device Name: 3 V Sin Sweep 1 Hz
File Path: D:\Feburary 2022\Charles\Electrode Reversal Tests
Automated: ●
Cycle Time (s): 60
Full save path:
Ao Channels: XDAQ_1/ao0
Ai Channels: XDAQ_1/ai0:15
Sampling Rate: 1000
N samples: 1000
Samples Per File: 1000000
Sample mode: Continuous
DAQ Trigger: /XDAQ_1/PXI_Trig0
Counter Resource: XDAQ_1/ctr0
SMU Channel: SMU_4ch
SMU Channel #: 2
Current Limit: 300.000u
Voltage Limit: 5.00000
Current Range: 300.000u
Voltage Range: 5.00000
SMU Mode: DC Voltage
Transient Response: Fast
Aperture Time: 100.000u
ResMeas Spike (V): 100.000m
ResMeas Width (s): 1.00000m
SMU Trigger: /SMU_4ch/PXI_Trig0
Signal Type: Waveform
Wave Function: Sine Wave
Phase (deg): 0
Frequency (Hz): 1
Offset (V): 0
Amplitude (V): 3
Duty Cycle %: 20
Seed: 0
Mean: 0
Std. Dev: 0
Idle Time (ms): 0
Pre-Width (ms): 0
Post-Width (ms): 0
Pre-Delay (ms): 0
Post-Delay (ms): 0
Pre-Amp (V): 0
Post-Amp (V): 0
Time (min): 0
Pulse Delay (ms): 0
Pulse Width (ms): 0
Row #: 0
Delay (ms): 0
Run #: 0
dt: 0
# of digits: 0
K size: 0
File Path: C:\Users\Gim\Desktop\data\June 2019\Epsilon
Append Signals: ●
DAQ Output #: 1
SMU Output #: 0
Idletime?: ●
Delay Points: 0
Delay Voltage: 0
Arb Samples: 1000
MNIST Digit
Pattern #: 1
Error Codes: status ● code 0

Figure 11. Overview of the LabVIEW software suite's graphical interface sourcing a 3 V 1 Hz sinusoidal wave into electrode 0 and the sink designated to electrode 5.

3.3 Electrical Properties of Neuromorphic Networks

Representative voltage-voltage responses of AgI and Ag_2Se networks are demonstrated in Figures 12 and 13 respectively. Each system bears its own unique non-linear switching properties. This distribution of various non-linear dynamics across the networks is an essential component for RC based in-materio computing in which the outputs should each bear their own level of unique complexity. The AgI networks notably have a prominent capacitive element in addition to their non-linearity which created even more uniquely distributed dynamics across the networks.

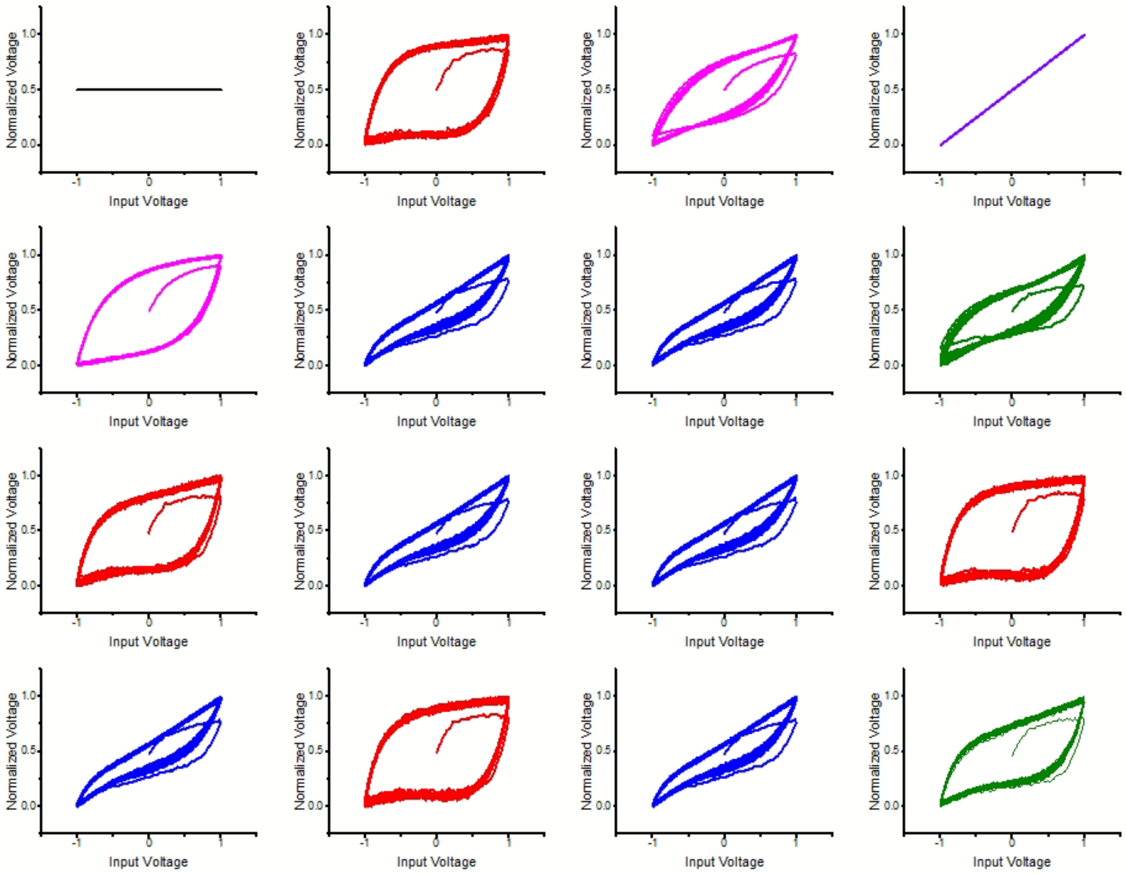

Figure 12. Lissajous plots highlighting the non-linear dynamics emergent within the AgI network under a 1 V, 7 Hz triangle wave sourced to electrode 3 and sink set to electrode 0. The capacitive properties of the network can clearly be observed in addition to its memristive non-linearity.

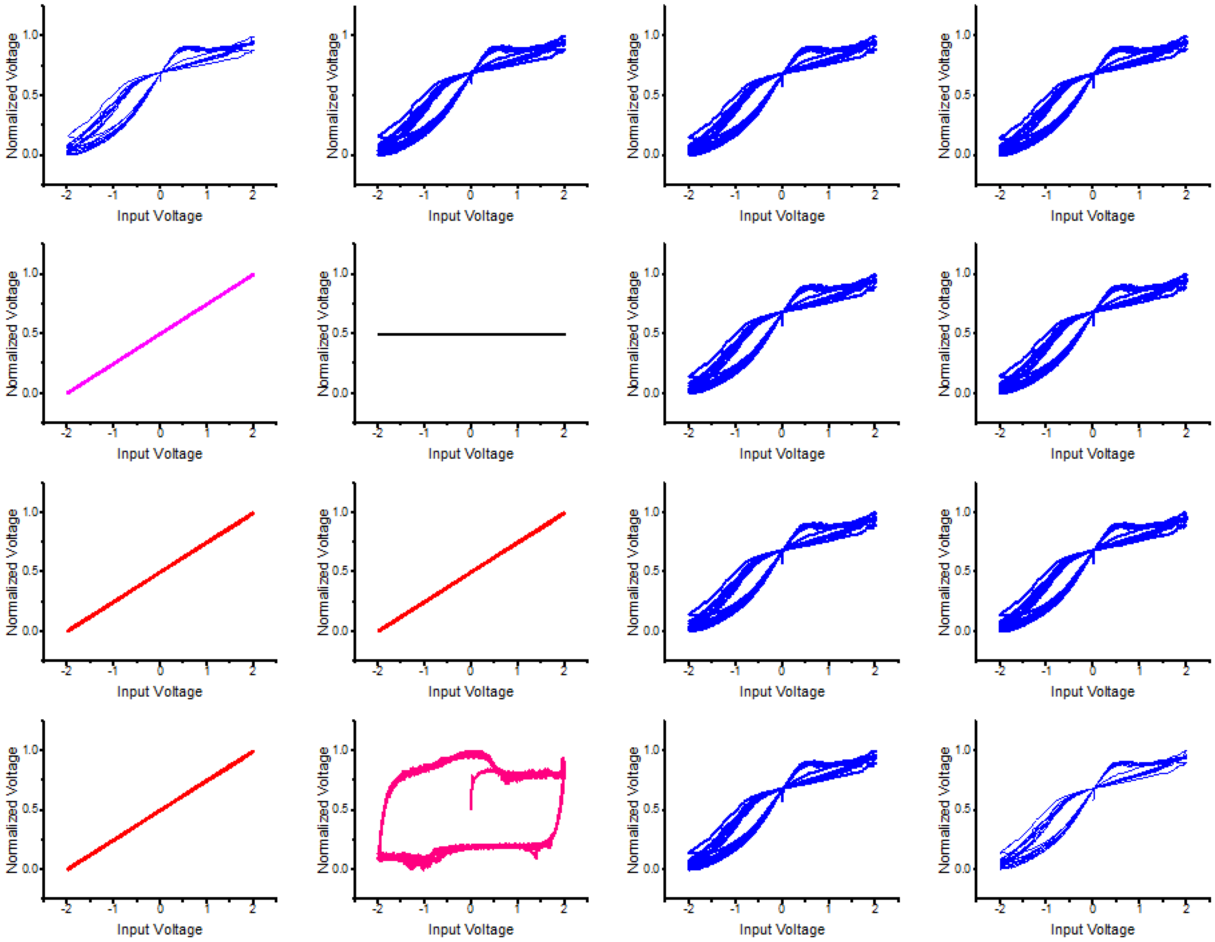

Figure 13. Lissajous plots highlighting the non-linear dynamics emergent within the Ag_2Se networks under a 2 V, 1 Hz triangle wave sourced to electrode 5 and sink set to electrode 6. The Ag_2Se exhibits more traditional memristive behavior distributed throughout the network though channels highlighted in red appear to be Ohmic.

Chapter 4:

Spoken Digit Classification

4.1 Modern Speech Recognition Techniques

Speech recognition is one of many fundamental tasks employed in the field of machine learning based natural language processing and has become ubiquitous in everyday technology[48]. Common approaches to speech recognition use algorithms to segment sections of raw audio data and bin them into hidden Markov models using a Markov chain approach[49]. Markov models are frequently used for processing stochastic time series data which assume that future data will be generated independent of the previous inputs[49]. While this technique has become highly effective, it has done so at the cost of becoming increasingly computationally expensive[3].

Emerging neural network models have demonstrated that they may be better suited to handle larger data sets at a reduced computational cost and are a promising candidate for the processing of dynamic time-series data[50]. Despite the improvements ANNs offer over Markov models, they continue to elicit a high computational demand. Implementing the ASN as a dynamic reservoir for RC offers the potential to alleviate the computational burden through in-materio computing. Herein, two classes of materials are explored within an ASN framework as potential candidates for in-materio RC spoken digit classification tasks.

4.2 Silver Iodide Network Results

The AgI networks were capable of achieving 95% accuracy of spoken digit classification across all input voltage ranges when taking linear regression of both the input and out layers (the full reservoir) as shown in Figure 14. Linear regression of the input layer alone provided worse accuracy with increasing points for regression as a consequence of overfitting. This further highlights the benefits of employing a dynamic reservoir to improve the efficiency of machine learning tasks. The systems accuracy of classifying tasks across a wide range of voltages, notably lower ones, is a further benefit towards lower power in-materio compute frameworks.

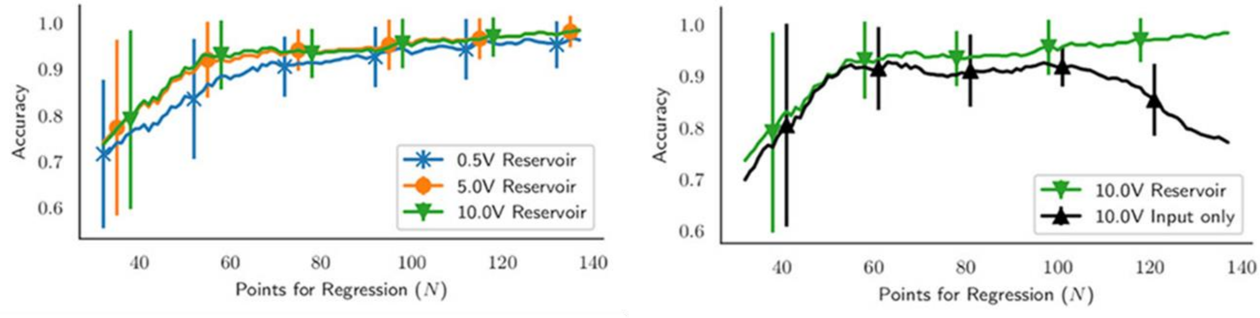

Figure 14. (Left) Reservoir's spoken digit accuracy of 95% across all possible voltage ranges of the DAC. (Right) Regression of the input layer shows overfitting with increasing points for regression while the reservoirs accuracy improves.

Spoken digit classification tasks were successfully realized in the AgI network through RC. Raw audio samples were provided from the free spoken digit database (FSDD), however the task was not performed on the raw audio data. The audio signal (Figure 15.) was pre-processed into Mel-frequency cepstrum coefficients (MFCC) which represent short-term power spectrums of the raw signal. This technique generates a non-linear representation of the frequencies that better approximate the auditory response in mammals and is commonly employed in the field of language processing[51,52].

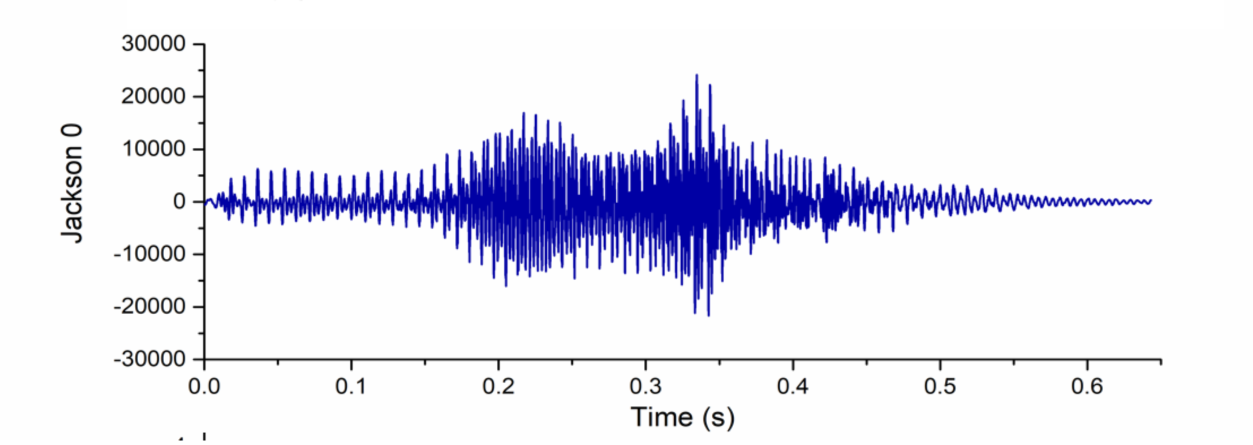

Figure 15. Raw audio data of speaker Jackson saying the digit zero.

The raw audio was first zero-padded and then segmented into a series of 25 ms windows spaced 10 ms apart. Each window was parametrized into 13 MFCCs for a total of 1,287 MFCCs. The array of MFCCs was flattened such that the lowest frequency coefficients were introduced into the ASN first followed by the highest as a voltage time series sampled at 1 kHz (Figure 16.). A sink was designated and all remaining 14 electrodes were left floating and their voltage outputs recorded. The recorded voltage traces were used for linear regression to discern which digit had been spoken. From the FSDD dataset speakers Jackson and Theo were selected having spoken the digits 0, 1 and 2. Two recordings of each digit from each speaker were employed. In addition to the 14 output electrodes, the input voltage trace was also used as a time series for regression.

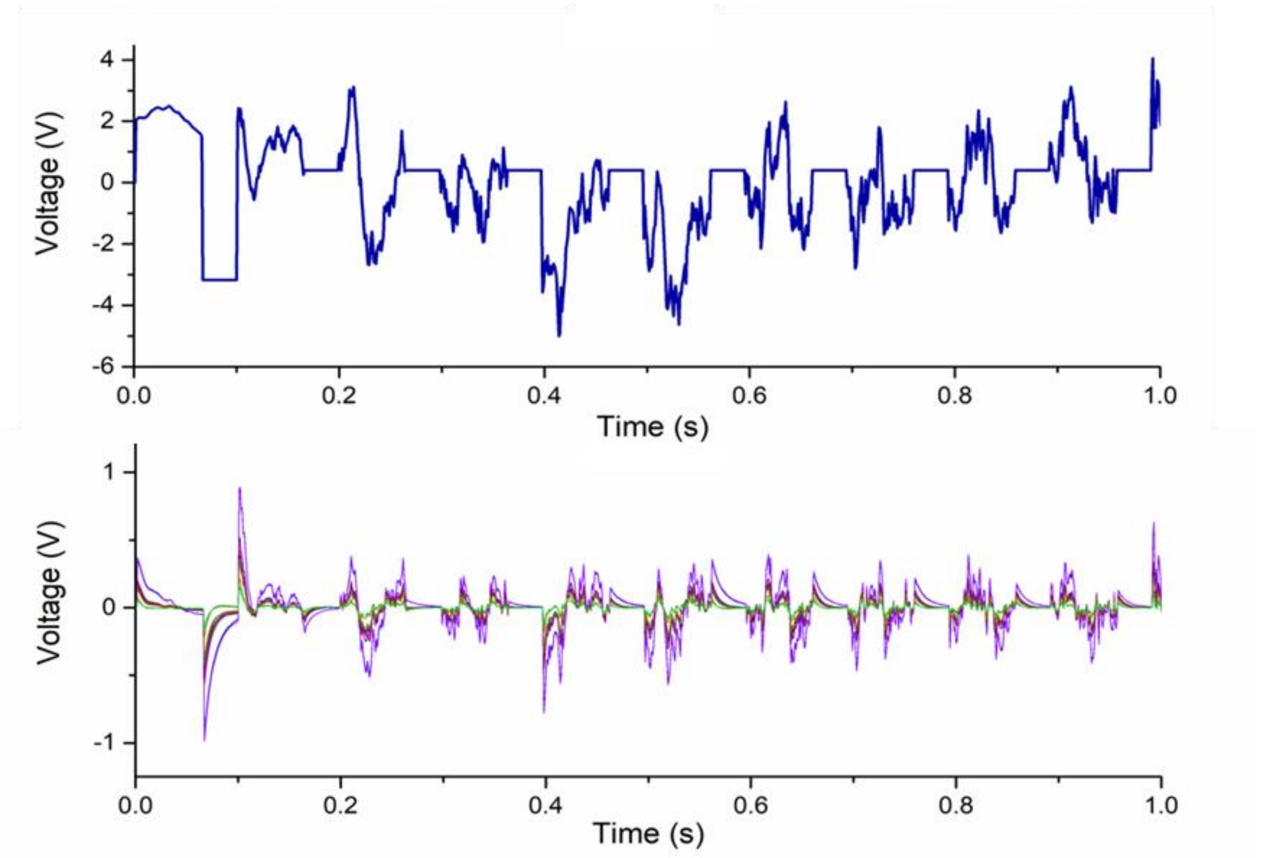

Figure 16. (Top) The MFCC converted signal of the raw audio data as voltage time-series to be fed into the network. (Bottom) Readout layer response of all 14 electrodes in response to the stimulus shows unique dynamic transformations of the parent signal.

4.3 Silver Selenide Network Results

The accuracy of Ag_2Se was surveyed across 10 digits and across 6 speakers to survey a wider range of datasets as shown in Figure 17. As with the AgI networks linear regression was performed on both the input signal (without device) and with the input and out signals (with device). An accuracy of 85% was achieved across all 10 digits spoke 50 times and across 6 different speakers saying the same digit with the output layer providing a noticeable improvement over regression of the input layer alone.

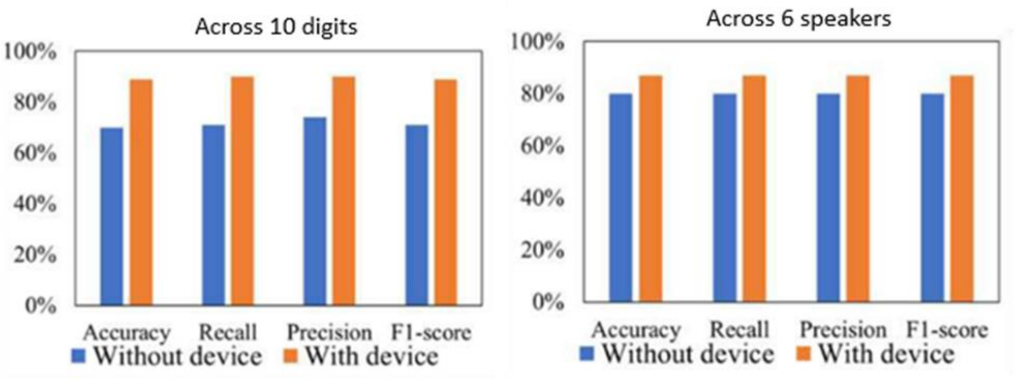

Figure 17. (Left) The Ag_2Se network's accuracy was 85% across all ten digits from a single speaker with equal accuracy in recalling information of previous inputs. The F1 score represents the mean harmonics between recall and precision. (Right) Accuracies of 82% were achieved in classifying a single spoken digit across six speakers with comparable recall and precision.

As with the AgI networks, raw audio data was provided from the FSDD. Fast Fourier transforms of the raw audio data were carried out as the pre-processing step and their corresponding frequency values were converted to their time dependent values. Only two output layers were used in contrast to the 14 in AgI networks. 80% of the output layer was used for training tasks with the remaining 20% utilized for the prediction tasks. Unlike the AgI network, a support vector machine was used as the classifier during the learning phase. The successful classification of spoken digits across different material networks strongly implicates neuromorphic nanowires as a viable, low power in-materio substrate for both existing and emergent machine learning frameworks.

Chapter 5:

Handwritten Digit Classification

5.1 Modern Image Recognition Techniques

The current state of image recognition techniques typically employs convolutional neural networks (CNNs)[53,54]. The CNNs are a modified class of ANNs which apply a technique called convolution in their layers in addition to the commonly used matrix multiplications in ANNs. CNNs are currently the state-of-the-art technique for image recognition tasks, however they rely on GPU based hardware to perform these complex tasks[55]. Consequently, the more complex the image recognition task is, higher computational demand and power consumption arise. The Modified National Institute of Standards and Technology (MNIST) handwritten digit database has become a standard, publicly available dataset which acts a benchmark task for image recognition techniques[56,57]. The MNIST database comprises 60,000 training images and 10,000 testing images. Each handwritten digit occupies a 28x28 pixel square grid with pixel intensity values ranging from 0 (dark) to 255 (bright). This dataset was used to assess the viability of employing a neuromorphic, in-materio RC framework for image recognition techniques. As with spoken digit classification tasks, this work implicates the utilization of an Ag_2Se network as an energy efficient alternative to CNN based classification techniques.

5.2 Silver Selenide Network MNIST Results

The Ag_2Se networks were able to successfully achieve 92% accuracy in classifying handwritten digits from MNIST as shown in Figure 18. Interestingly, despite having 14 potential readout layers, accuracy saturated after using 7 of the total readouts (Figure 18.) suggesting that these networks don’t necessarily require scaling up to improve efficiency. Through a self-supervised online learning technique, the network was able to reach its maximum accuracy through the training of only 2000 digits. This reduction in training dataset sizes is another example of the optimal properties which emerge from in-materio RC and further suggests larger size MEAs may not be a requirement for achieving higher accuracies.

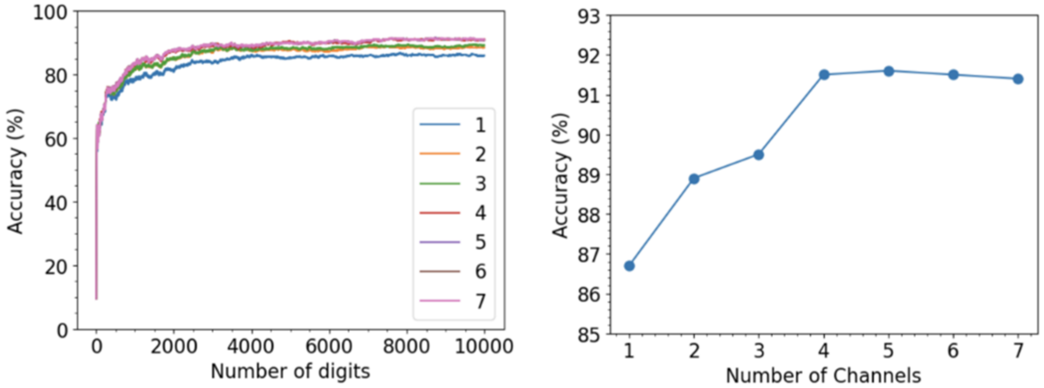

Figure 18. (Left) Accuracy of MNIST classification as a function of number of digits used for training and readout layers used demonstrates 92% accuracy after 2000 digits. (Right) Maximum accuracy of MNIST as a function of readout layers used shows a saturation of accuracy with 7 electrodes.

By further probing the dynamics of the Ag_2Se network, a technique for assessing the quality of each electrode was derived through examining the mutual information (MI) between readout electrodes. Mutual information is a dimensionless quantity that measures a relationship between two variables which have been sampled at the same time. For a given readout electrode, there exists a degree of MI between it and other readout electrode responses to a given input digit. The MI between each individual readout relative to an input digit is shown to be directly correlated with its classification accuracy. By taking the mean of this MI between electrodes, it becomes apparent that electrodes with a higher degree of MI exhibit higher accuracies as shown in Figure 19. The MI between electrodes directly maps onto the dynamics of the networks as cab seen by the MI’s relationship the Lissajous plots of all readout electrodes.

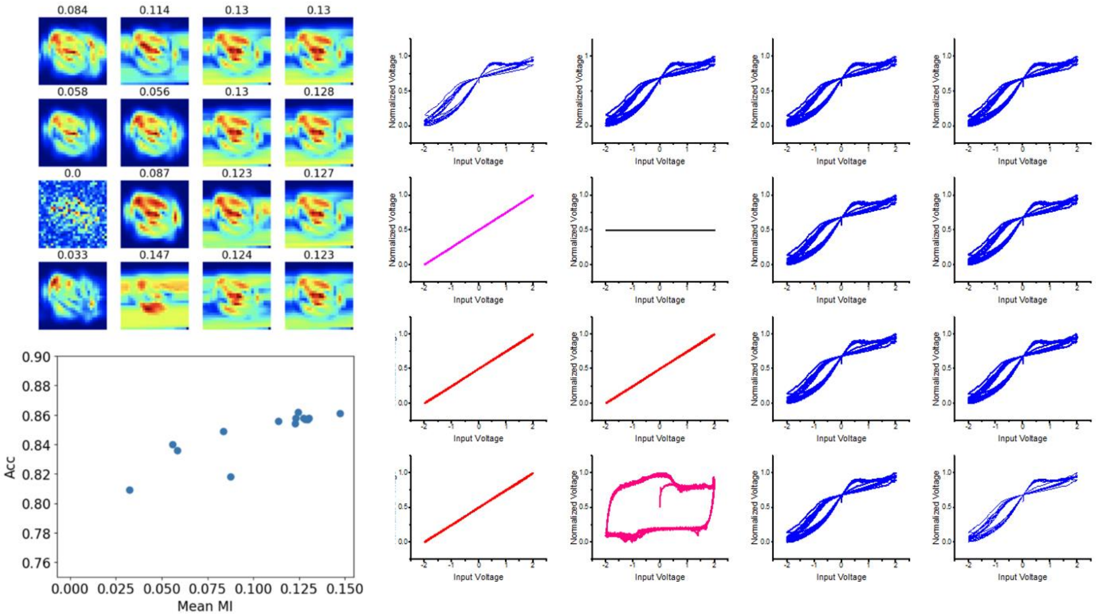

Figure 19. (Left) MI between all electrodes showing heat map regions of higher mean mutual information. A linear increase in accuracy as a function of MI can be observed from individual readout electrodes suggesting more dynamic channels have better accuracies. (Right) The Lissajous plots exhibiting non-linear dynamics from Figure X. appear to directly map onto regions of higher MI.

To introduce the handwritten digits into the network, the 28x28 arrays are converted into a 1x784 array of values ranging from 0-255. The pixel intensity values are then normalized to correspond to input voltages ranging from -X to +Y or from 0 to ± X (Figure 20.). These signals are then fed into the network 2000 digits at a time and sampled at 10 kHz with each digit corresponding to a 784 ms segment of the time-series. The non-linear dynamic responses in conjunction with memory of previous inputs can also be directly observed from the readout voltage responses of any given digit (Figure 20.).

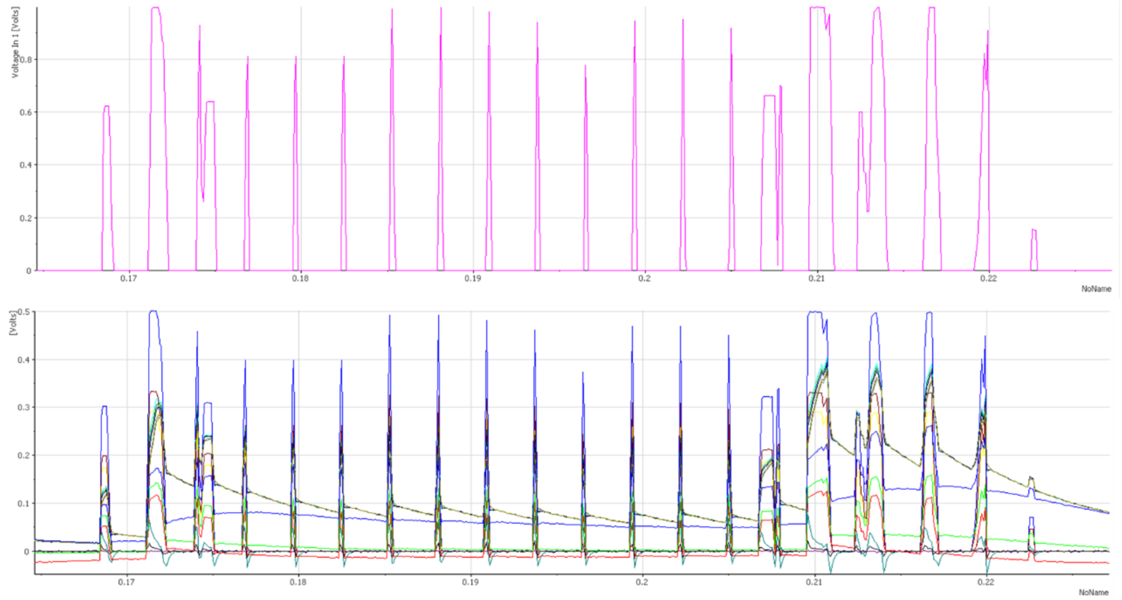

Figure 20. (Top) Input voltage trace of the digit 5 with pixel intensities normalized to a range of 0 to 1 volts. (Bottom) All 14 readout electrode's voltage traces as a response to input digit 5.

Unlike the spoken digit recognition tasks, this approach utilizes a shallow online learning technique on the output layers which requires only a single epoch to achieve high accuracies as shown in Equation 6.

$$W\Lambda = Y \qquad (6)$$

The sample space is denoted by the matrix Λ shown in equation 7 where each column (a_i) represents a single sample comprising M features. A second matrix Y shown in equation 8 is employed for the labels corresponding to the samples with N representing the number of classes in the dataset.

$$\Lambda = [a_1, a_2, \ldots, a_k], \Lambda \in \mathbb{R}^{M\times k} \qquad (7)$$

$$Y = [y_1, y_2, \ldots, y_k], Y \in \mathbb{R}^{M\times k} \qquad (8)$$

This method uses Tapson's modification of Greville's iterative algorithm to compute a pseudoinverse[58]. This yields a self-supervised, online learning algorithm which generates a pseudoinverse solution from the linear system shown in equation 6. The solutions to the algorithm are constantly updated with each new sample making this a suitable method for real-time computing tasks.

While this technique employs an algorithm that is traditionally more computationally expensive than linear regression, it only requires a single epoch to achieve 92% handwritten digit classification accuracy. This both implicates the networks as a suitable framework for in-materio RC and also as a potential hardware accelerator for software-based machine learning algorithms.

The successful implementation of the ASN framework for hand written digit classification techniques further demonstrates that neuromorphic nanowires are a promising candidate to be implemented in more complex, emergent machine learning tasks while offering lower power consumption than traditional software-based algorithms which rely on von Neumann architectures. Further classes of memristive materials should be explored in the ASN framework as potential alternative candidates for optimizing in-materio based RC applications.

Chapter 6:

Neuromorphic Networks and Criticality

6.1 Overview of Critical Dynamics

There is an abundance of collective systems in nature that demonstrate behaviors which appear to behave in an unpredictable manner differing from their individual elements[59–61]. Such a phenomenon is classified as emergent behavior which arises when properties of a collection of elements which cannot be predicated from any individual element in the system[62]. The observation of this anomaly has sparked a desire to discern the mechanisms responsible for these complex dynamics. One proposed mechanism of interest is that mammalian brains and other complex systems are exhibiting criticality[63]. This theory postulates that the collection of elements exists at a critical point in which they operate between disordered and ordered states analogous to a phase transition. Critical systems are interesting and unique in that they exhibit spatio-temporal interactions over very wide scale ranges.

There are five fundamental properties which should be exhibited by a critical system. (i) A critical system should follow a power law relationship (equation 9) between its order and control parameters in addition to the size of the system. Power law scaling had previously thought to be a sole criterion for criticality, though that has since been challenged[64,65].

$$p(x) \;\; \alpha \;\; x^{-\beta} \qquad (9)$$

(ii) There should be a finite size scaling of the order parameter’s susceptibility relative to its correlation length. (iii) There must exist a mathematical relationship between the exponents of the power-law across different parameters in a dynamic system[66,67]. (iv) The system should demonstrate evidence of shape collapse such that multiple events across varying scales exhibit similar properties[66]. (v) The control parameters of the system must be capable of tuning the system into or out of critically dynamic regimes[67]. These notable criteria have become a major point of focus on recent experimental studies concerning critical systems[68].

It has been hypothesized that criticality is a driving factor in the emergent properties of neuromorphic nanowire networks. Characteristic properties of criticality had previously been observed in Ag_2S networks[26]. Notably they have exhibited variable modulations in conductance over long time scales with power-law fittings of the networks power spectral density spanning over multiple decades of frequencies. Recent experiments with silver-polyvinylpyrrolidone based networks have also demonstrated that they exhibit properties of avalanche criticality[69]. The properties of the Ag_2Se networks were also recently explored beyond their RC applications and implicated as an abiotic system for studying tunable critical dynamics.

6.2 Critical Dynamics in Neuromorphic Ag_2Se Networks

The observation of memristive behavior is consistently exhibited by Ag_2Se networks across numerous cycles (Figure 21.). Certain intervals throughout the network demonstrate the occasional presence of hard switching events which correspond to sharp, abrupt changes in conductance. Notably, each cycle exhibits its own unique non-linear response to the input signal as a consequence of its fading memory properties and the non-equilibrium dynamics inherent to the system. Through repeated cycles the current-voltage response of the network begins to occupy a localized phase-space. This property of the networks suggests that chaotic attractor dynamics are present within these dynamic frameworks and consequently, the noise inherent to this system is amplified and may even act as a driving force within the network[69]. Further experiments employing Lyapunoc exponent analysis are warranted to determine if these non-linear, dynamic responses are the result of an edge-of-chaos state.

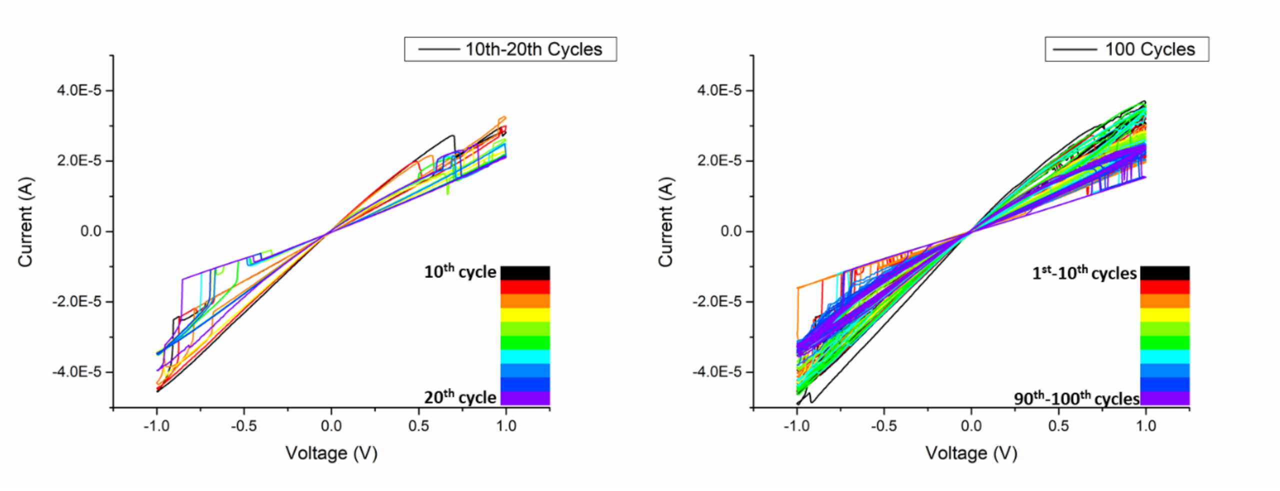

Figure 21. Current-voltage response of the network under a 1 V, 1 Hz triangle wave exhibits characteristic memristive switching properties in addition to chaotic attractor dynamics as more cycles are fed into the network. (Left) Cycles 10-20. (Right) Cycles 1-100.

Going beyond the non-linear dynamics in response to an AC signal, the networks also exhibit a modulation of conductance under a DC stimulus across large time scales. The network's unique response to a simple DC signal suggests that while the networks appear to approach a steady state, they never fully achieve a thermodynamic equilibrium. Current fluctuations in response to a DC signal often exhibit avalanches, or current fluctuations beyond a defined threshold of 5% of the mean. The power spectral density of these current traces exhibit a power-law trend as can be observed in Figure 22.

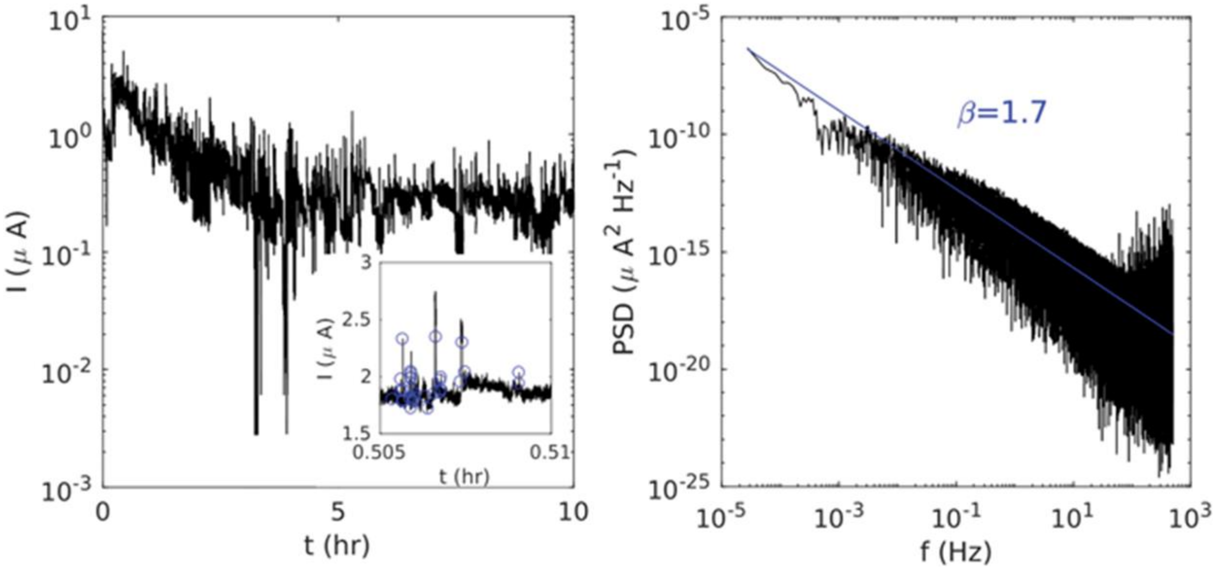

Figure 22. (Left) Current time-series of the Ag_2Se network stimulated under a 5 V DC bias for 10 hours still exhibits persistent conduction fluctuations from switching events. The inset shows regions in which the deviation in current exceeds a set 5% threshold (Right) Power-spectral density of the network and its power law fit (blue line).

The avalanche events of the network under a DC bias are further probed and determined to fit within power-law scaling. The avalanches probability distributions were calculated as a function of size (S), avalanche duration (T) and the average avalanche size $\langle S \rangle$. The exponents of the maximum likelihood of a certain power-law were determined for P(S) and P(T) and were $\tau_S = 1.89 \pm .002$ and $\tau_T = 2.21 \pm .04$ respectively. The exponent of $\langle S(T) \rangle$ was calculated to be $\gamma = 1.23 \pm 0.04$ and is consistent with the predicted values for a crackling noise dynamic scaling relationship (Figure 23.). These properties confirm avalanche criticality within the network with the critical exponent $\gamma = 1.23$ differing from the power spectral density exponent $\beta = 1.7$ which further confirms the inhomogeneous nature of these neuromorphic networks.

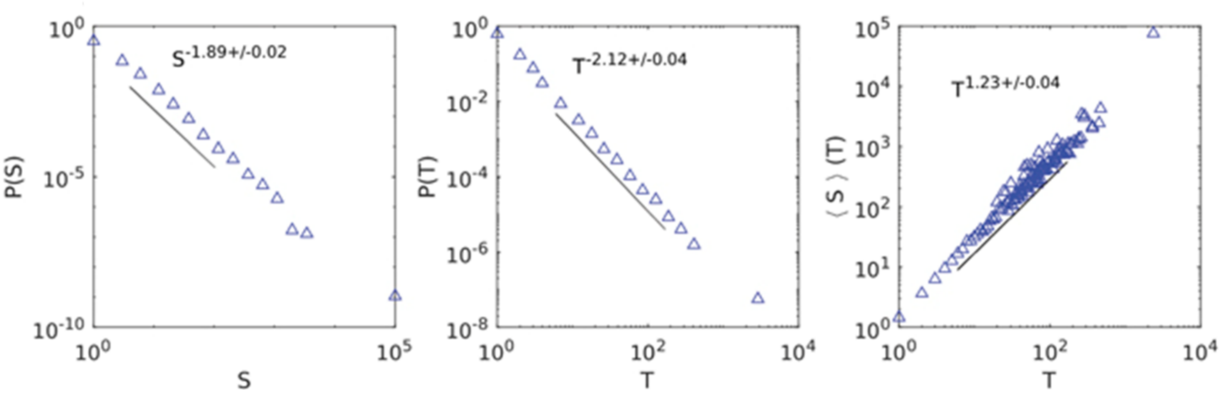

Figure 23. Probability distributions (triangles) and power-law fitting of DC stimulated avalanches (line) from the current time series. (Left) Size of avalanches. (Middle) Duration of avalanches. (Right) Average avalanche size as a function of T.

The Ag_2Se neuromorphic nanowire networks exhibit the requisite properties for avalanche criticality in addition to its intrinsic memristive properties. The observation of these properties implicate the ASN framework as an abiotic system which can be employed to study the properties of critical systems. Additionally, chaotic attractor dynamics have been observed to be present within the networks over large time scales spanning across days. The unique properties inherent to these networks warrants further investigations to discern how and why these critical properties may relate to the intrinsic computational capabilities of ASN frameworks.

Chapter 7:

Atomically Precise Manufacturing

7.1 History of 3D Printing Techniques

The advent of 3D printing, a form of additive manufacturing, is still relatively new and was first proposed by Murray Leinster's novel First Contact in 1945. It wasn't until 26 years later when Teletype Corporation first invented inkjet technology in 1971 which was able to extract material through a nozzle[70]. This was the first rendition of printing technology as a whole and pioneered the development of modern day desktop printers. That same year, Johannes F. Gottwald patented the liquid metal recorder which would use melted wax driven through a nozzle to pave way towards the printing of materials other than inks[71]. The advent of this technology stagnated for a decade until Hideo Kodama filed for a patent in 1981 that envisioned using a photosensitive plastic which could harden in the presence of light[72].

A year later Raytheon filed a patent for the use of metal powders as a means of combining layers of materials. In 1984 the term 3D printing was first coined in a patent by Bill Masters where he foresaw the use of computer automated systems to drive 3D printing technology[73]. The same year Chuck Hull developed the first 3D printer dubbed the stereolithographic apparatus which greatly improved the throughput over cruder attempts to realize 3D printing and was commercialized in 1989[74]. Unfortunately, this emerging technology was cost prohibitive and only industrial facilities could typically afford them. The next decade saw an explosion in patents filed for 3D printing technologies and various models of 3D printers were explored, though they were difficult to print with high fidelity[75]. It was in 1997 when the first metal materials were 3D printed by AeroMat through a technique called laser additive manufacturing in which a laser was employed to melt titanium alloy powders[76]. The Wake Forest Institute of Regenerative Medicine grew the first 3D printed organ, a bladder which was implanted into a human test subject in 1999[77]. In 2005 RepRap was conceived as an open source initiative to develop more affordable 3D printers and the first commercial printer was released in 2008 under the RepRap initiative[78]. It wasn't until 2009 that commercial products like the MakerBot Cupcake CNC and its successor the Thing-O-Matic became more commonplace[78]. That same year saw the birth of online crowdfunding platforms which resulted in a steep rise in the development of these technologies as hobbyists and researchers alike began funding and fabricating newer printers like the Form 1 in 2021 or the Buccaneer in 2013[78]. Two years later Cellink produced the first standardized, commercial 3D printer capable of using a seaweed based bio-ink for printing tissue cartilage and this technology is still utilized in modern day research[79,80].

Researchers have been meticulously studying the applications of 3D printing in parallel to their historical development as there is an insurmountable demand for the use 3D printers in the manufacture of biological specimens, metallic materials, electronic devices and other potential commercial materials[81–84].

7.2 3D Printing Techniques in Modern Manufacturing

The allure of being able to fabricate and manufacture materials with the utmost of freedom has garnered a large amount of interest within the industrial and medical communities. The idea that a machine could print an organ viable for transport, complex geometry-based components for spacecraft and even intricate concrete structures was once nothing short of science fiction. The continued research and development of 3D printing technologies has grown in parallel with researchers and manufacturers ever increasing demands[85,86].

As of 2019, the aerospace industry accounts for a whopping 18.2% of the additive manufacturing market[87]. This is a consequence of their high demand for materials which necessitate complex geometries to facilitate air flow and heat dissipation. Additionally, many of the ceramic and alloy-based materials implemented into spacecraft are incredibly difficult to machine[88]. Recent advances have made the fabrication of metallic components easier, though ceramics and other materials derived from nanostructures still pose a notable difficulty due to the environments influence on finished products[89]. Current studies envision the realization of on-demand fabrication of parts within a space ship in addition to the automated repairing of materials[88].

Likewise, the biomedical industry also must deal with the burden of trying to manufacture incredibly complex drugs and organs suitable for transplant into humans[88,90]. The desire to print organs is of notable interest as current transplant patients are required to wait for other human organ donors. Various human tissues have successfully been printed including skin tissues, livers and gall bladders[88]. However, vascular systems which facilitate blood flow have posed great difficulties in the 3D organ printing paradigm[91]. The successful realization of 3D printing techniques for the aforementioned applications necessitates the development of more rigid and precise tools which can be readily applied to both biological and inorganic frameworks.

7.3 Towards Atomically Precise Manufacturing

The first STM was developed by Gerd Binning and Heinrich Rohrer and it achieved molecular resolution of silicon atoms in 1981 and their first publication of surface images from CaIrSn4 (110) and Au(110) was released a year later[92]. The operating principle of STM takes advantage of quantum mechanics, specifically electron tunneling as a consequence of wave-particle duality. Eight years after the first STM was developed, Don Eigler demonstrated that atoms could be manipulated laterally on a substrate. This was first demonstrated by the spelling of IBM out of 35 xenon atoms in 1989[93]. In 1996 James K. Gimzewski created an operational abacus using C_{60} molecules on a Cu(111) substrate[94]. In-situ polymerization has also performed as a means of chemical soldering in 2011, implicating the STM as an atomically resolved medium to facilitate chemical reactions[95]. A stop motion movie titled *A Boy and His Atom* was even created at IBM using carbon monoxide molecules which was released to the public in 2013**.** Recent advances in the automation of scanning probe microscopes has led to the development of atomic silicon logic gates in 2018[96]. While the lateral manipulation of atoms and molecules has been repeatedly demonstrated throughout the years in conjunction with STM facilitating chemical reactions, to date there have been no successful techniques developed which are capable of also manipulating atoms in the Z direction to create 3D objects[97].

Atomically precise manufacturing aims to leverage scanning probe microscopy techniques to develop additive (or subtractive) manufacturing of 3D materials with atomic precision[98]. The realization of APM will require the development of surface bound molecular tools to act as additive and subtractive mediums. An ideal molecular tool should exhibit three key components. First, the molecule should rigidly adhere to the surface employed. This can be achieved by synthesizing tripodal legs onto a molecular framework. Second, the molecule should possess a rigid cage-like structure to host the legs, ideally in a tetrahedral symmetry such that a bridgehead position is available. Third, the bridgehead position of the molecular cage should contain a reactive headgroup which can be manipulated either electrochemically and/or mechanically. The headgroup will act as the essential defining element of any unique molecular tool. This headgroup should possess a chemically weak, reactive bond which can generate a surface bound radical. The radical should be tailored such that it will bind to the tip when they are brought into a close proximity together and the bond formed will be stronger than the bond to be broken. Based on the desired task this can be utilized to either abstract or donate atoms and molecules to or from the tip to the molecular tool.

Gold surfaces are commonly employed as a substrate for STM experiments and the characterization of molecules deposited onto its surface. Consequently, the packing and properties of thiol-based molecules have been extensively explored on single gold crystal surfaces[99,100]. Unlike most molecules which are weakly adsorbed to unreactive gold surfaces by van der Waals forces in STM, thiols are also capable of chemisorbing to unoccupied high energy sites[101,102]. This is a highly desirable property which can be leveraged when developing the "feet" of the molecular tool's tripods and will be employed in the development of the tool's anchoring properties.

Adamantane cages are the simplest building blocks of diamond and nanodiamond structures[103]. They are comprised entirely of covalent hydrocarbon bonds and form a rigid, relatively inert cage structure. The rigid nature of this structure in conjunction with its tetrahedral symmetry implicate adamantane as a suitable candidate for the cage structure of the molecular tools. The tetrahedral symmetry enables the formation of tripodal legs with a bridgehead position vacant for the addition of the reactive headgroup and thiolated variants of these molecules have been extensively studied within STM experiments[104].

Carbon-halide bonds (other than fluorine) are relatively weak and easy to break. They also have a rich history of being used in substitution reactions within the field of organic chemistry[105]. Halides of particular interest are bromine and iodine as they form the weakest carbon-halide bonds and their bond enthalpies are lower than any other bonds present in the adamantane cage. A C-Br bond is selected for the bridgehead position to act as an abstraction tool.

The electrochemical and/or mechanical manipulation of the molecule should enable the removal of bromine and the generation of a surface bound radical at the bridgehead position of the adamantane cage. This adamantane radical has been demonstrated to be stable at lower temperatures (77 K) and unreactive to oxygen[106]. The atom to be abstracted from the STM tip will then be brought within close proximity of this radical and used to form a C-Au bond, breaking the Au-Au bonds present in the tip, ultimately extracting a single gold atom. With these properties in mind, the molecular tool 1-Bromo-3,5,7-tris(mercaptomethyl)adamantane (BATT) was synthesized and employed as abstraction tool (Figure 24.).

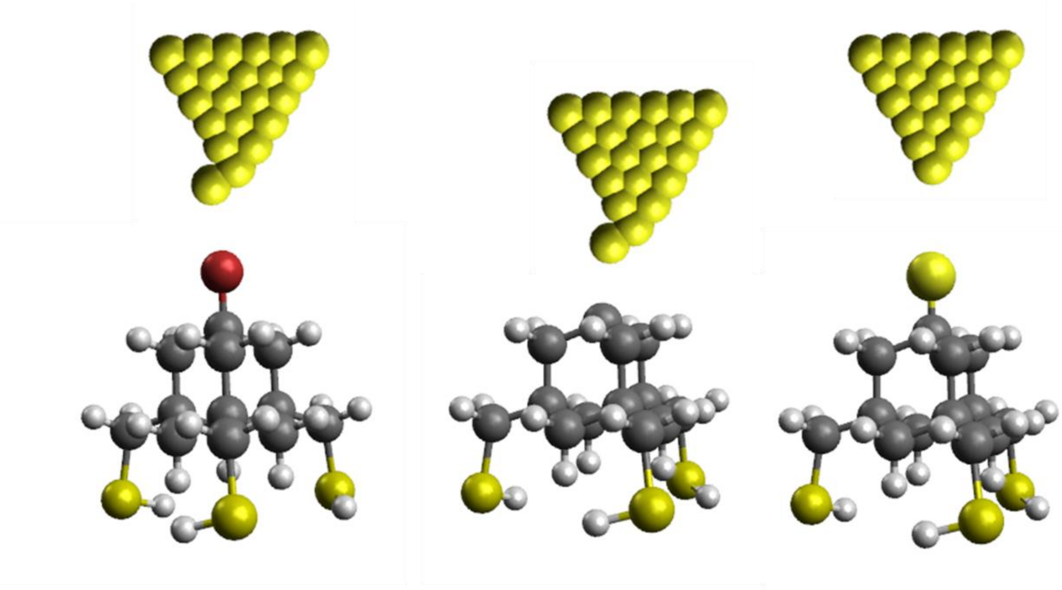

Figure 24. Workflow for atomically resolved abstraction. (Left) Constant current regulation is turned off and the tip with defects is driven 300 pm towards the surface with an increased gap voltage of -3 V to generate a surface bound radical. (Middle) The tip defect is positioned over the surface bound radical and driven towards it without regulation. (Right) Simulations suggest upon reaching a distance of 3.2 Å the tip defect will jump from the tip to the surface bound radical, terminating it with the abstracted defect.

7.4 Preliminary Results of APM Experiments

The packing of molecular tools can be observed in Figures 25-27, where submonolayer coverage shows the BATT preferentially sitting on the high energy kinks in the herringbones of the gold surface. The BATT molecules also decorate the entirety of atomic steps and all observed monolayers appeared to emerge from atomic steps.

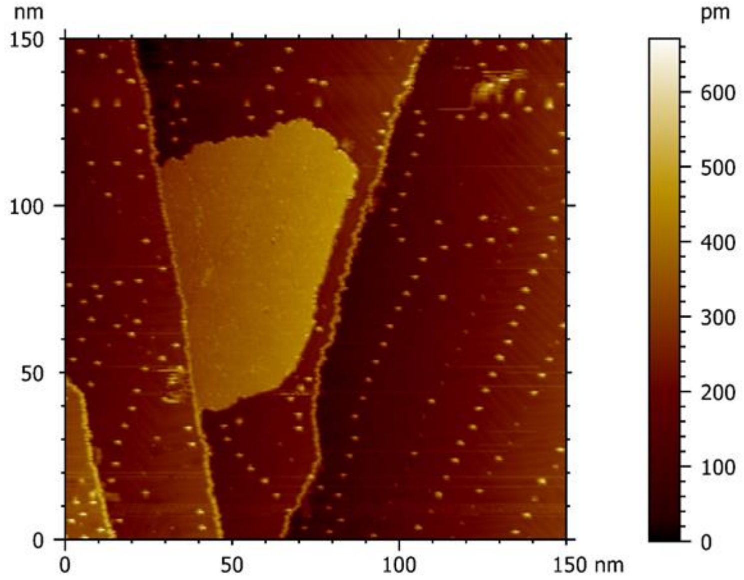

Figure 25. Zoomed out 150 nm scan showing both submonolayer and monolayer packing of the BATT molecules at 78 K with monolayers emerging from BATT decorated atomic steps and individual molecules packing at the herringbone kinks (tunnel conditions I_t = 150 pA, V_{gap} = -850 mV).

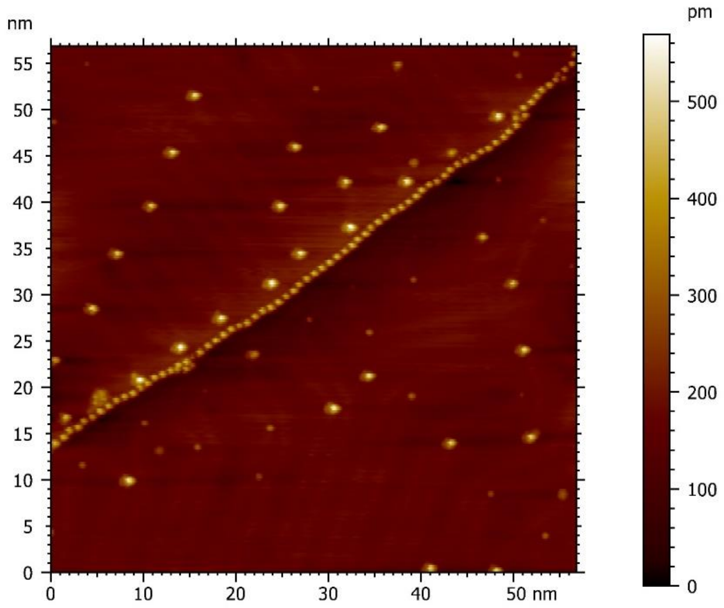

Figure 26. Zoomed in 50 nm scan showing submonolayer coverage of BATT along herringbone kinks and packing along the atomic steps (tunnel conditions I_t = 200 pA, V_{gap} = -800 mV).

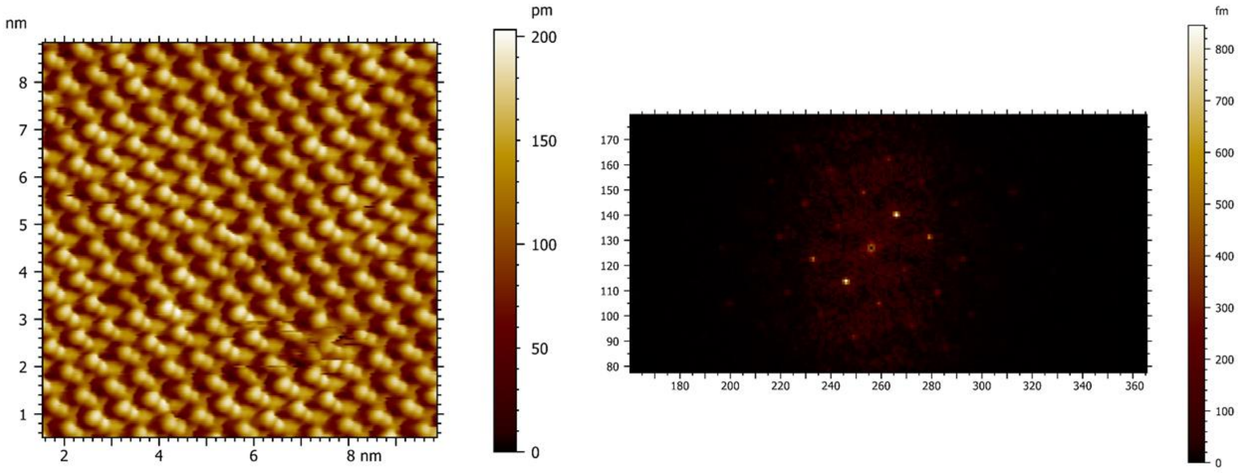

Figure 27. (Left) 10 nm scan of the BATT shows its molecular packing in a monolayer (tunnel conditions I_t = 200 pA, V_{gap} = -1.3 V). (Right) FFT spectrum of the monolayer.

The debromination of the BATT was reproducibly carried out by changing the gap voltage of the system and Z driving the tip towards the apex of the molecule. The gap voltage is temporarily modified to -3 volts and the tip is driven 300 pm towards the molecule without current regulation to remove the bromine atoms. This approach leverages the electro-mechano breaking of a relatively weak C-Br bond in the BATT in conjunction with the relative stability of adamantane radicals.

Experimental results directly align with theoretical calculations as can be seen in Figures 28 and 29. While it is difficult to characterize surface bound radicals in an STM environment, theoretical calculations suggest that these electrochemical, mechanosynthetic approaches should yield highly reactive molecules for the abstraction or donation of desired atoms/molecules. Further experiments demonstrating the abstraction of atoms from the tip using the BATT molecules are warranted.

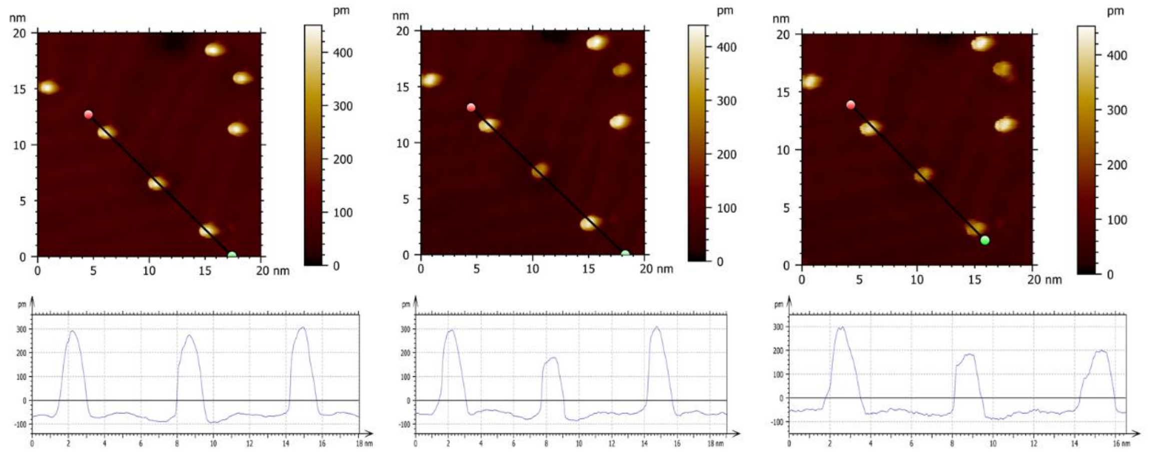

Figure 28. (Top, left to right) Experimental sequential debromination of BATT molecules demonstrates the reproducible removal of bromine atoms (tunnel conditions I_t = 100 pA, V_{gap} = -700 mV). (Bottom, left to right) Line profiles of the apparent height of BATT prior to and after debromination show a reproducible apparent height difference.

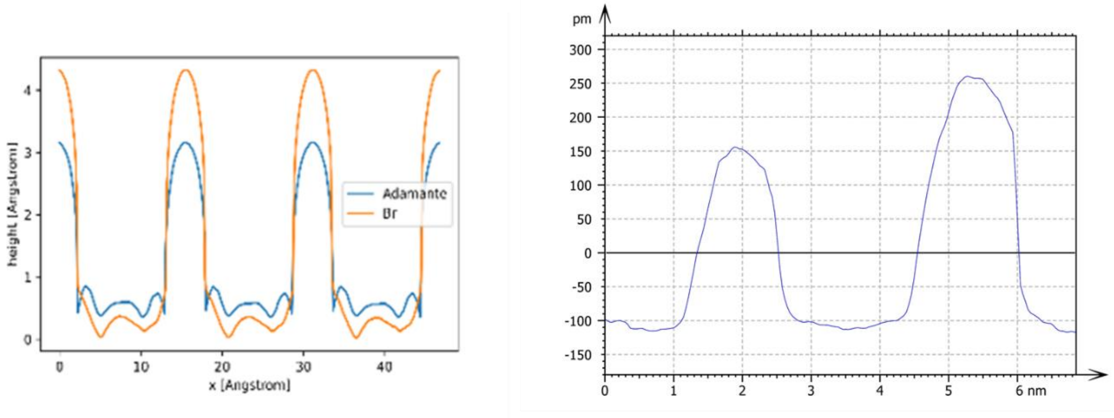

Figure 29. Theoretical calculations of the apparent height of the BATT molecule (orange line, 384.8 pm) and the debrominated BATT (blue line, 254.6 pm) directly align with experimental observations of the apparent height from BATT (359.8 pm) and debrominated BATT (253.8 pm).

Future work aims to selectively positon tip defects over the surface bound radical for atomically resolved abstraction. Consequently, the tall protrusion of the C-Br bond relative to the surface has been demonstrated to act as a molecular probe capable of imaging scanning probe tips. The apparent geometry of the molecule changes in appearance after tip forming procedures as can be seen in Figure 30. To confirm this phenomenon, the data was post-processed through full blind tip deconvolution methods using Mountains SPIP 9 software. The tip deconvolution algorithm uses distorted features from the STM image to approximate in the tip geometry. Across all samples of BATT, SPIP tip deconvolution implicates the scanning probe tip as looking identical to the "molecule" on the surface. The ability of the BATT molecule to image scanning probe tips in real-time is another added benefit that will aid in streamlining the process of sequentially removing tip defects and could be paired with machine learning algorithms towards automation of this technique.

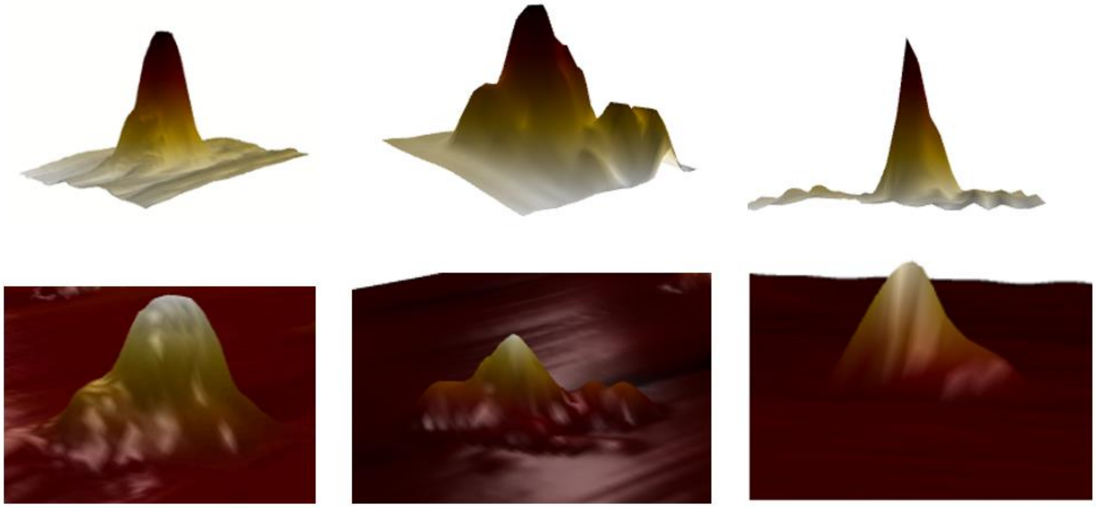

Figure 30. (Top row) Post-processed full blind tip deconvolutions of the BATT molecule with different tip geometries directly align with (Bottom row) experimental images of the "BATT molecule" demonstrating BATT's capability of performing real-time tip imaging.

7.5 STM Methodology

All STM measurements were carried out using a commercially purchased LT STM III and its corresponding vacuum chamber from Scienta Omicron. Custom preparation chambers and load locks were designed to interface with the microscope chamber. Each chamber comprises a roughing line, turbo pump and ion pump, though the load lock doesn't employ an ion pump. The custom load lock enables for sample transfer in a UHV environment while the custom preparation chamber allows for in-situ cleaning of substrates. Tungsten tips were etched in 0.6 M KOH and characterized under an optical microscope prior to introduction into the vacuum environment. Clean gold samples were prepared by repeated ion gun Ar^+ sputtering (1.5 kV, 5E-5 Torr) and indirect heating anneal cycles (350^o C) and was confirmed by STM imaging using a freshly etched W tip. For deposition of BATT, the molecule was isolated by a gate valve and preheated to 80^o C for 5 minutes to purify the sample. The gate valve was then opened and the sample was exposed to the subliming BATT for 40 seconds. STM images confirmed this technique offers a reproducible deposition of submonolayer coverage onto the gold substrate.

Chapter 8:

Conclusions

Neuromorphic nanowires networks composed of AgI and Ag_2Se have been implicated as suitable physical substrates for in-materio RC. Both materials exhibit the requisite properties for RC frameworks including the non-linear transformation of input signals into higher dimensionality, separable readout layers and fading memory properties. The ASN framework is a promising candidate towards implementing hardware capable of performing memory and logic operations in parallel. The utilization of a physical materials intrinsic capacity to perform computational tasks greatly alleviates the burden of training costs in conventional ANN algorithms while also significantly reducing the energy consumed during training.

The ASN has successfully performed spoken digit classification tasks through in-materio RC with accuracies of up to 95% across two different memristive materials. Silver selenide networks were also employed for hand written digit classification tasks and achieved accuracies of up to 92%. The high accuracies achieved in these proof-of-concept experiments strongly suggest that the ASN framework may be a suitable low power alternative to traditional natural language processing and computer vision-based machine learning tasks.

The dynamics of the ASN were further probed to elucidate the origins of its emergent non-linear properties. The ASN's dynamic, non-linear response to input signals have been experimentally discerned to be the consequence of avalanche criticality. The critical properties of these networks is strongly believed to be an influencing factor on the ASN's intrinsic capacity to perform computational tasks. However, it is still unclear as to why the critical nature of the neuromorphic networks corresponds to its suitability for in-materio RC applications and further investigation into this phenomenon is warranted.

Scanning probe microscopy techniques have also been explored and implicated as a potential system for enabling APM. Through the meticulous design of molecular tools, we demonstrate that a reactive headgroup of a molecular tool can be reproducibly removed through electro-mechanochemistry. Consequently, the BATT molecule has demonstrated its capability to perform real-time tip imaging tasks which will enable confirmation of atomic abstraction in real-time. The successful realization of molecular tripods with rigid adamantane cages suggests various different head groups could be designed for the donation or abstraction of atoms or molecules between the STM tip and the tool. Future studies on this subject are warranted to fully develop a platform capable of achieving 3D printing techniques with atomic precision.

References

1. Jordan, M. I. & Mitchell, T. M. Machine learning: Trends, perspectives, and prospects. *Science* vol. 349 255–260 (2015).

2. Holzinger, A., Kieseberg, P., Weippl, E. & Tjoa, A. M. Current advances, trends and challenges of machine learning and knowledge extraction: From machine learning to explainable AI. in *Lecture Notes in Computer Science (including subseries Lecture Notes in Artificial Intelligence and Lecture Notes in Bioinformatics)* vol. 11015 LNCS 1–8 (Springer Verlag, 2018).

3. Mehonic, A. & Kenyon, A. J. Brain-inspired computing needs a master plan. *Nature* **604**, 255–260 (2022).

4. Strubell, E., Ganesh, A. & Mccallum, A. *Energy and Policy Considerations for Deep Learning in NLP*. https://bit.ly/2JTbGnI (2019).

5. Strubell, E., Ganesh, A. & McCallum, A. Energy and policy considerations for modern deep learning research. in *AAAI 2020 - 34th AAAI Conference on Artificial Intelligence* vol. 34 1393–13696 (AAAI press, 2020).

6. Thompson, N. C., Greenewald, K., Lee, K. & Manso, G. F. Deep Learning's Diminishing Returns: The Cost of Improvement is Becoming Unsustainable. *IEEE Spectr.* **58**, 50–55 (2021).

7. Lopes, N., Ribeiro, B. & Quintas, R. GPUMLib: A new library to combine Machine Learning algorithms with Graphics Processing Units. in *2010 10th International Conference on Hybrid Intelligent Systems, HIS 2010* 229–232 (2010).

8. AI and Compute. https://openai.com/blog/ai-and-compute/.

9. Talati, N. *et al.* mMPU—A Real Processing-in-Memory Architecture to Combat the von Neumann Bottleneck. in *Springer Series in Advanced Microelectronics* vol. 63 191–213 (Springer Verlag, 2020).

10. Kulkarni, M. S. & Teuscher, C. Memristor-based reservoir computing. in *Proceedings of the 2012 IEEE/ACM International Symposium on Nanoscale Architectures, NANOARCH 2012* 226–232 (IEEE Computer Society, 2012).

11. Hasegawa, T., Terabe, K., Tsuruoka, T. & Aono, M. Atomic Switch: Atom/Ion Movement Controlled Devices for Beyond Von-Neumann Computers. *Adv. Mater.* **24**, 252–267 (2012).

12. Chua, L. O. Memristor—The Missing Circuit Element. *IEEE Trans. Circuit Theory* **18**, 507–519 (1971).

13. Strukov, D. B., Snider, G. S., Stewart, D. R. & Williams, R. S. The missing memristor found. *Nature* **453**, 80–83 (2008).

14. Stathopoulos, S. *et al.* Multibit memory operation of metal-oxide Bi-layer memristors. *Sci. Rep.* **7**, 1–7 (2017).

15. Kitaev, A. Y. Quantum computations: algorithms and error correction. *Russ. Math. Surv.* **52**, 1191–1249 (1997).

16. Ohno, T. *et al.* Sensory and short-term memory formations observed in a Ag2S gap-type atomic switch. *Appl. Phys. Lett.* **99**, (2011).

17. Chang, T. & Jo, S. Short-Term Memory to Long-Term Memory Transition in a Nanoscale Memristor. *ACS Nano* (2011).

18. Williams, R. How we found the missing memristor. *Spectrum, IEEE* **45**, 28–35 (2008).

19. Vlasov, A. I. *et al.* Entrepreneurship and Sustainability Issues Market for Memristors and Data Mining Memory Structures For Promising Smart Systems. **8**, (2020).

20. Avizienis, A. V *et al.* Neuromorphic atomic switch networks. *PLoS One* **7**, e42772--e42772 (2012).

21. Türel, Ö., Lee, J. H., Ma, X. & Likharev, K. K. Neuromorphic architectures for nanoelectronic circuits. *Int. J. Circuit Theory Appl.* **32**, 277–302 (2004).

22. Stuart, C., Park, H.-K. & Chen, Y. Fabrication of a 3D Nanoscale Crossbar Circuit by Nanotransfer-Printing Lithography. *Small* **6**, 1663–1668 (2010).

23. Xia, Q. & Yang, J. J. Memristive crossbar arrays for brain-inspired computing. *Nature Materials* vol. 18 309–323 (2019).

24. Alibart, F., Zamanidoost, E. & Strukov, D. B. Pattern classification by memristive crossbar circuits using ex situ and in situ training. *Nat. Commun.* **4**, (2013).

25. Stieg, A. Z. *et al.* Self-organized atomic switch networks. *Japanese Journal of Applied Physics* vol. 53 01AA02 (2014).

26. Stieg, A. Z. *et al.* Emergent Criticality in Complex Turing B-Type Atomic Switch Networks. *Adv. Mater.* **24**, 286–293 (2012).

27. Wang, S.-C. Artificial Neural Network. in *Interdisciplinary Computing in Java Programming* 81–100 (Springer US, 2003).

28. Nakajima, K. & Fischer, I. *Natural Computing Series Reservoir Computing Theory, Physical Implementations, and Applications*. http://www.springer.com/series/4190.

29. Tanaka, G. *et al.* Recent advances in physical reservoir computing: A review. *Neural Networks* vol. 115 100–123 (2019).

30. Verstraeten, D., Schrauwen, B., Stroobandt, D. & Van Campenhout, J. Isolated word recognition with the Liquid State Machine: A case study. *Inf. Process. Lett.* **95**, 521–528 (2005).

31. Lilak, S. *et al.* Spoken Digit Classification by In-Materio Reservoir Computing With Neuromorphic Atomic Switch Networks. *Front. Nanotechnol.* **3**, 38 (2021).

32. Scharnhorst, K., Woods, W., Teuscher, C., Stieg, A. & Gimzewski, J. Non-Temporal logic performance of an atomic switch network. in *Proceedings of the IEEE/ACM International Symposium on Nanoscale Architectures, NANOARCH 2017* 133–138 (Institute of Electrical and Electronics Engineers Inc., 2017).

33. Demis, E. C. *et al.* Nanoarchitectonic atomic switch networks for unconventional computing. *Jpn. J. Appl. Phys.* **55**, 1102B2 (2016).

34. Zahlten, C. *et al.* High-NA EUV lithography: pushing the limits. in *35th European Mask and Lithography Conference (EMLC 2019)* (eds. Behringer, U. F. & Finders, J.) vol. 11177 43 (SPIE, 2019).

35. Erdmann, A., Mesilhy, H. & Evanschitzky, P. Attenuated phase shift masks: a wild card resolution enhancement for extreme ultraviolet lithography? *J. Micro/Nanopatterning, Mater. Metrol.* **21**, 020901 (2022).

36. Terabe, K., Hasegawa, T., Nakayama, T. & Aono, M. Quantized conductance atomic switch. *Nature* **433**, 47–50 (2005).

37. Aguilera, R. *et al.* Atomic Switch Networks for Neuroarchitectonics: Past, Present, Future. in 201–243 (Springer, Cham, 2020).

38. Sillin, H. O. *et al.* A theoretical and experimental study of neuromorphic atomic switch networks for reservoir computing. *Nanotechnology* **24**, (2013).

39. Kotooka, T. *et al.* Ag2Se Nanowire Network as an Effective In-Materio Reservoir Computing Device. (2021) doi:10.21203/rs.3.rs-322405/v1.

40. Avizienis, A. V. *et al.* Morphological transitions from dendrites to nanowires in the electroless deposition of silver. *Cryst. Growth Des.* **13**, 465–469 (2013).

41. Bharathi Mohan, D., Sreejith, K. & Sunandana, C. S. Surface plasmon-exciton transition in ultra-thin silver and silver iodide films. *Appl. Phys. B Lasers Opt.* **89**, 59–63 (2007).

42. Gnanavel, M. & Sunandana, C. S. Optical absorption and photoluminescence in ultra thin silver and silver iodide films. in *2008 IEEE PhotonicsGlobal at Singapore, IPGC 2008* (2008).

43. Kato, Y. *et al.* Silver Iodide Formation in Methyl Ammonium Lead Iodide Perovskite Solar Cells with Silver Top Electrodes. *Adv. Mater. Interfaces* **2**, (2015).

44. Chen, H., Shin, D. W., Nam, J. G., Kwon, K. W. & Yoo, J. B. Selenium nanowires and nanotubes synthesized via a facile template-free solution method. *Mater. Res. Bull.* **45**, 699–704 (2010).

45. Mayers, B. T., Liu, K., Sunderland, D. & Xia, Y. Sonochemical synthesis of trigonal selenium nanowires. *Chem. Mater.* **15**, 3852–3858 (2003).

46. Elizondo, D. The linear separability problem: Some testing methods. *IEEE Transactions on Neural Networks* vol. 17 330–344 (2006).

47. Singh, V. K. Proposing Solution to XOR Problem Using Minimum Configuration MLP. in *Procedia Computer Science* vol. 85 263–270 (Elsevier B.V., 2016).

48. Kanabur, V., Harakannanavar, S. S. & Torse, D. An Extensive Review of Feature Extraction Techniques, Challenges and Trends in Automatic Speech Recognition. *Image, Graph. Signal Process.* **5**, 1–12 (2019).

49. Mor, B., Garhwal, S. & Kumar, A. A Systematic Review of Hidden Markov Models and Their Applications. *Arch. Comput. Methods Eng.* **28**, 1429–1448 (2021).

50. Mustafa, M. K., Allen, T. & Appiah, K. A comparative review of dynamic neural networks and hidden Markov model methods for mobile on-device speech recognition. *Neural Comput. Appl.* **31**, 891–899 (2019).

51. Han, W., Chan, C. F., Choy, C. S. & Pun, K. P. An efficient MFCC extraction method in speech recognition. in *Proceedings - IEEE International Symposium on Circuits and Systems* 145–148 (2006).

52. Gupta, K. & Gupta, D. An analysis on LPC, RASTA and MFCC techniques in Automatic Speech recognition system. in *Proceedings of the 2016 6th International Conference - Cloud System and Big Data Engineering, Confluence 2016* 493–497 (Institute of Electrical and Electronics Engineers Inc., 2016).

53. Li, Y. Research and Application of Deep Learning in Image Recognition. in 994–999 (Institute of Electrical and Electronics Engineers (IEEE), 2022).

54. Chauhan, R., Ghanshala, K. K. & Joshi, R. C. Convolutional Neural Network (CNN) for Image Detection and Recognition. in *ICSCCC 2018 - 1st International Conference on Secure Cyber Computing and Communications* 278–282 (Institute of Electrical and Electronics Engineers Inc., 2018).

55. Yao, C. *et al.* Evaluating and analyzing the energy efficiency of CNN inference on high-performance GPU. *Concurr. Comput. Pract. Exp.* **33**, e6064 (2021).

56. Deng, L. The MNIST database of handwritten digit images for machine learning research. *IEEE Signal Process. Mag.* **29**, 141–142 (2012).

57. Cohen, G., Afshar, S., Tapson, J. & Van Schaik, A. EMNIST: Extending MNIST to handwritten letters. in *Proceedings of the International Joint Conference on Neural Networks* vols 2017-May 2921–2926 (Institute of Electrical and Electronics Engineers Inc., 2017).

58. Tapson, J. & van Schaik, A. Learning the pseudoinverse solution to network weights. *Neural Networks* **45**, 94–100 (2013).

59. Brown, J. H. *et al.* The fractal nature of nature: Power laws, ecological complexity and biodiversity. *Philos. Trans. R. Soc. B Biol. Sci.* **357**, 619–626 (2002).

60. Arthur, W. B. Complexity and the Economy. in *Handbook of Research on Complexity* (Edward Elgar Publishing)..

61. Foote, R. Mathematics and complex systems. *Science* vol. 318 410–412 (2007).

62. Zhengping, L., Cheng, H. S. & Malcolm, Y. H. L. A survey of emergent behavior and its impacts in agent-based systems. in *2006 IEEE International Conference on Industrial Informatics, INDIN'06* 1295–1300 (IEEE Computer Society, 2006).

63. Cocchi, L., Gollo, L. L., Zalesky, A. & Breakspear, M. Criticality in the brain: A synthesis of neurobiology, models and cognition. *Progress in Neurobiology* vol. 158 132–152 (2017).

64. Stumpf, M. P. H. & Porter, M. A. Critical truths about power laws. *Science* vol. 335 665–666 (2012).

65. Touboul, J. & Destexhe, A. Power-law statistics and universal scaling in the absence of criticality. *Phys. Rev. E* **95**, 012413 (2017).

66. Friedman, N. *et al.* Universal critical dynamics in high resolution neuronal avalanche data. *Phys. Rev. Lett.* **108**, 208102 (2012).

67. Beggs, J. M. & Timme, N. Being critical of criticality in the brain. *Front. Physiol.* **3 JUN**, 163 (2012).

68. Dunham, C. S. *et al.* Nanoscale neuromorphic networks and criticality: a perspective. *J. Phys. Complex.* **2**, 042001 (2021).

69. Hochstetter, J. *et al.* Avalanches and edge-of-chaos learning in neuromorphic nanowire networks. *Nat. Commun.* **12**, 1–13 (2021).

70. He, G. & Li, Y. Study on the Development of Inkjet Imaging Digital Printing Technology Based on Patent Analysis. in 168–179 (Springer, Singapore, 2022).

71. Gottwald, J. F. Liquid Metal Recorder. Patent US3596285A. (1971).

72. Kodama, H. Automatic method for fabricating a three-dimensional plastic model with photo-hardening polymer. *Rev. Sci. Instrum.* **52**, 1770–1773 (1981).

73. Masters, W. E. Computer automated manufacturing process and system. Patent US4665492A. (1987).

74. Hull, C. W. Apparatus for production of three-dimensional objects by stereolithography . US4575330A. (1984).

75. Su, A. & Al'Aref, S. J. History of 3D printing. in *3D Printing Applications in Cardiovascular Medicine* 1–10 (Elsevier, 2018).

76. Ninpetch, P., Kowitwarangkul, P., Mahathanabodee, S., Chalermkarnnon, P. & Ratanadecho, P. A Review of Computer Simulations of Metal 3D Printing. *AIP Conference Proceedings* **2279**, 50002 (2020).

77. Whitaker, M. The history of 3D printing in healthcare. *Bull. R. Coll. Surg. Engl.* **96**, 228–229 (2014).

78. Horvath, J. A Brief History of 3D Printing. in *Mastering 3D Printing* 3–10 (Apress, 2014).

79. Berglund, L., Rakar, J., Junker, J. P. E., Forsberg, F. & Oksman, K. Utilizing the Natural Composition of Brown Seaweed for the Preparation of Hybrid Ink for 3D Printing of Hydrogels. *ACS Appl. Bio Mater.* **3**, 6510–6520 (2020).

80. İyigün, İ. & Görçün, Ö. F. *Logistics 4.0 and Future of Supply Chains*. (Springer Singapore, 2022).

81. Schniederjans, D. G. Adoption of 3D-printing technologies in manufacturing: A survey analysis. *Int. J. Prod. Econ.* **183**, 287–298 (2017).

82. Murr, L. E. Frontiers of 3D Printing/Additive Manufacturing: from Human Organs to Aircraft Fabrication. *Journal of Materials Science and Technology* vol. 32 987–995 (2016).

83. Espera, A. H., Dizon, J. R. C., Chen, Q. & Advincula, R. C. 3D-printing and advanced manufacturing for electronics. *Progress in Additive Manufacturing* vol. 4 245–267 (2019).

84. Murphy, S. V. & Atala, A. 3D bioprinting of tissues and organs. *Nature Biotechnology* vol. 32 773–785 (2014).

85. Gopinathan, J. & Noh, I. Recent trends in bioinks for 3D printing. *Biomaterials Research* vol. 22 1–15 (2018).

86. Tay, Y. W. D. *et al.* 3D printing trends in building and construction industry: a review. *Virtual Phys. Prototyp.* **12**, 261–276 (2017).

87. Najmon, J. C., Raeisi, S. & Tovar, A. Review of additive manufacturing technologies and applications in the aerospace industry. in *Additive Manufacturing for the Aerospace Industry* 7–31 (Elsevier Inc., 2019).

88. Ngo, T. D., Kashani, A., Imbalzano, G., Nguyen, K. T. Q. & Hui, D. Additive manufacturing (3D printing): A review of materials, methods, applications and challenges. *Composites Part B: Engineering* vol. 143 172–196 (2018).

89. Ivanova, O., Williams, C. & Campbell, T. Additive manufacturing (AM) and nanotechnology: Promises and challenges. *Rapid Prototyp. J.* **19**, 353–364 (2013).

90. Kang, H. W. *et al.* A 3D bioprinting system to produce human-scale tissue constructs with structural integrity. *Nat. Biotechnol.* **34**, 312–319 (2016).

91. Hann, S. Y. *et al.* Recent advances in 3D printing: vascular network for tissue and organ regeneration. *Translational Research* vol. 211 46–63 (2019).

92. Binning, G., Rohrer, H., Gerber, C. & Weibel, E. Surface studies by scanning tunneling microscopy. *Phys. Rev. Lett.* **49**, 57–61 (1982).

93. Toumey, C. 35 atoms that changed the nanoworld. *Nature Nanotechnology* vol. 5 239–241 (2010).

94. Cuberes, M. T., Schlittler, R. R. & Gimzewski, J. K. Room-temperature repositioning of individual C60 molecules at Cu steps: Operation of a molecular counting device. *Appl. Phys. Lett.* **69**, 3016–3018 (1996).

95. Okawa, Y. *et al.* Chemical wiring and soldering toward all-molecule electronic circuitry. *J. Am. Chem. Soc.* **133**, 8227–8233 (2011).

96. Huff, T. *et al.* Binary atomic silicon logic. *Nat. Electron.* **1**, 636–643 (2018).

97. Lutz, C. & Gross, L. 30 years of moving individual atoms. *Europhys. News* **51**, 26–28 (2020).

98. Randall, J. N. *et al.* Digital atomic scale fabrication an inverse Moore's Law – A path to atomically precise manufacturing. *Micro and Nano Engineering* vol. 1 1–14 (2018).

99. Häkkinen, H. The gold-sulfur interface at the nanoscale. *Nature Chemistry* vol. 4 443–455 (2012).

100. Love, J. C., Estroff, L. A., Kriebel, J. K., Nuzzo, R. G. & Whitesides, G. M. Self-Assembled Monolayers of Thiolates on Metals as a Form of Nanotechnology. (2005)

101. Guo, Q. & Li, F. Self-assembled alkanethiol monolayers on gold surfaces: Resolving the complex structure at the interface by STM. *Phys. Chem. Chem. Phys.* **16**, 19074–19090 (2014).

102. Vericat, C., Vela, M. E., Benitez, G., Carro, P. & Salvarezza, R. C. Self-assembled monolayers of thiols and dithiols on gold: new challenges for a well-known system. *Chem. Soc. Rev.* **39**, 1805–1834 (2010).

103. Ekimov, E. A. *et al*. High-Pressure, High-Temperature Synthesis of Nanodiamond from Adamantane. *Inorg. Mater*. **55**, 437–442 (2019).

104. Hohman, J. N., Claridge, S. A., Kim, M. & Weiss, P. S. Cage molecules for self-assembly. in *Materials Science and Engineering R: Reports* vol. 70 188–208 (Elsevier, 2010).

105. Hamlin, T. A., Swart, M. & Bickelhaupt, F. M. Nucleophilic Substitution (SN2): Dependence on Nucleophile, Leaving Group, Central Atom, Substituents, and Solvent. *ChemPhysChem* **19**, 1315–1330 (2018).

106. Tabushi, I., Aoyama, Y., Kojo, S., Hamuro, J. & Yoshida, Z. I. Free-Radical Halogenation of Adamantane. Selectivity and Relative Lifetime of 1- and 2-Adamantyl Radicals. *J. Am. Chem. Soc.* **94**, 1177–1183 (1972).